## Post-Print

This is the accepted version of:

# Shock Absorber Leakage Impact on Aircraft Lateral Stability During Ground Handling Maneuvers

José Joaquín Mendoza Lopetegui [*], Gianluca Papa [†], Marco Morandini [‡] and Mara Tanelli [§]

*Polytechnic University of Milan, 20133 Milan, Italy*

**Aircraft braking maneuvers are safety-critical on-ground motions that exhibit complex dynamics and significant dependence on system operating conditions. The fundamental interface between the aircraft and the ground is the landing gear. Among the landing gear components, the shock absorbers may be subject to gas leakage during their lifetime, which is an anomaly that could compromise the lateral stability properties of the aircraft on the operating regimes found during braking maneuvers. In this paper, an explicit link is established between Main Landing Gear shock absorber leakage and aircraft lateral stability. To investigate lateral stability, a high fidelity multibody nonlinear aircraft simulator is developed in a MATLAB/Simulink framework and validated against experimental data. To generate insight into the problem and to quantify shock absorber leakage impact on aircraft lateral stability, two simple but descriptive analytical models are also developed, each one on a different operating mode of the system. The analysis of the models reveals that shock absorber leakage can have a significant effect on aircraft lateral stability, especially at high velocities and highly damped nose wheel steering conditions. The models developed in this work may be used by aircraft control system designers to come up with more effective lateral stability controllers in the event of Main Landing Gear shock absorber leakage.**

**Nomenclature**

| Variable | Description | SI unit |
|----------|-------------|---------|
| $\beta$ | Aircraft body side-slip angle | rad |
| $v_a$ | Aircraft body velocity | m/s |
| $S$ | Aircraft front transversal surface | $m^2$ |

Continued on next page

[*] PhD Candidate, Department of Electronics, Information and Bioengineering, josejoaquin.mendoza@polimi.it (Corresponding Author).
[†] PhD Fellow, Department of Electronics, Information and Bioengineering, gianluca.papa@polimi.it.
[‡] Professor, Department of Aerospace Science and Technology, marco.morandini@polimi.it.
[§] Professor, Department of Electronics, Information and Bioengineering, mara.tanelli@polimi.it.

| Variable | Description | SI unit |
|---|---|---|
| $m_a$ | Aircraft mass | kg |
| $J_s$ | Aircraft front rotational joint moment of inertia | kg $m^2$ |
| $J_G$ | Aircraft moment of inertia around the vertical axis | kg $m^2$ |
| $\rho$ | Air mass density | kg/$m^3$ |
| $p_0$ | Air pressure at fully extended position | Pa |
| $V_0$ | Air volume at fully extended position | $m^3$ |
| $i_b$ | Braking current | A |
| $\mu_b$ | Braking pads friction coefficient | - |
| $A_p$ | Braking pads surface area | $m^2$ |
| $P_b^r, P_b^l$ | Braking pressures, right and left MLG sides | Pa |
| $T_b^r, T_b^l$ | Braking torques, right and left MLG sides | Nm |
| $\theta_i$ | Burckhardt friction parameters | - |
| $C_f$ | Cornering-stiffness on the front side | N |
| $C_r$ | Cornering-stiffness on the rear side | N |
| $v_c$ | Critical velocity | m/s |
| $\xi$ | Current valve damping coefficient | - |
| $\tau$ | Current valve delay | s |
| $\omega_n$ | Current valve undamped natural frequency | Hz |
| $C_c$ | Damping penetration factor | Ns/m |
| $\Delta F_b$ | Differential braking force | N |
| $c_d$ | Discharge coefficient | - |
| $l_f$ | Distance from front wheel to center of gravity | m |
| $l_l$ | Distance from rear wheels to aircraft longitudinal plane | m |

| Variable | Description | SI unit |
|---|---|---|
| $l_r$ | Distance from rear wheels to center of gravity | m |
| $C_D$ | Drag coefficient | - |
| $F_{drag}$ | Drag force | N |
| $R_{eff}$ | Effective radius of the disc brake | m |
| $\delta_f$ | Front steering angle | rad |
| $c_s$ | Front steering wheel rotational damping | Nm/(rad/s) |
| $g$ | Gravity acceleration | m/$s^2$ |
| $\rho_h$ | Hydraulic fluid mass density | kg/$m^3$ |
| $F_h$ | Hydraulic force | N |
| $a_y$ | Lateral acceleration | m/$s^2$ |
| $F_{yr}, F_{yf}$ | Lateral contact force, rear and front sides | N |
| $V_y$ | Lateral velocity | m/s |
| $C_L$ | Lift coefficient | - |
| $F_x$ | Longitudinal contact force | N |
| $\lambda^r, \lambda^l$ | Longitudinal wheel slips, right and left MLG sides | - |
| $A_n$ | Net orifice area | $m^2$ |
| $N_p$ | Number of braking pistons | - |
| $N_s$ | Number of braking pads per piston | - |
| $\delta_z$ | Penetration displacement | m |
| $\dot{\delta}_z$ | Penetration velocity | m/s |
| $A$ | Piston cross-sectional area | $m^2$ |
| $F_e$ | Pneumatic force | N |
| $n$ | Polytropic coefficient | - |

| Variable | Description | SI unit |
|---|---|---|
| $\delta_r$ | Rear disturbance steering angle | rad |
| $\omega$ | Rotational wheel speed | rad/s |
| $\mu$ | Runway friction coefficient | - |
| $\alpha_f$ | Side-slip angle on the front wheel | rad |
| $\alpha_r$ | Side-slip angle on the rear wheel | rad |
| $K_c$ | Stiffness penetration factor | N/m |
| $s$ | Stroke | m |
| $\dot{s}$ | Stroke speed | m/s |
| $d$ | Trailing arm length | m |
| $K_u$ | Under-steering gain | $s^2/m^2$ |
| $v_r, v_f$ | Velocity vectors, rear and front sides | m/s |
| $F_z$ | Vertical load | N |
| $c$ | Viscous damping coefficient | $Ns^2/m^2$ |
| $L$ | Wheelbase | m |
| $r$ | Wheel radius | m |
| $\psi$ | Yaw | rad |
| $\dot{\psi}$ | Yaw rate | rad/s |

## I. Introduction

EFFECTIVE and efficient aircraft on-ground operation is a challenging problem due to the complexities related to system dynamics, environmental factors, and pilot interaction. A particularly safety-critical class of aircraft on-ground motion are braking maneuvers, which may arise after a conventional landing, or after a Rejected Take-Off (RTO) in which the take-off is aborted at a significant velocity, requiring a quick aircraft stoppage. During a braking maneuver, maintaining lateral stability is of paramount importance for the safety of the pilot and for high performance operation. Therefore, a better understanding of aircraft lateral stability in these operating regimes is fundamental in

4

developing techniques to preserve stability during operation. Among the multiple factors that may impact aircraft lateral stability are system parameter variations. During the operational life of the system, the highly dynamic nature of a braking maneuver involves significant variations in terms of aircraft payload configurations, runway conditions, aerodynamic forces, and velocity regimes. An additional factor that will inevitably impact the properties of the system is component degradation. Of particular relevancy for lateral stability is the condition of the landing gear. Despite the efforts in the industry, landing gear failure is still among the common causes of aircraft failures [1]. One of the landing gear components that requires significant maintenance is the shock absorber, which is subject to oil and gas leakages during its operational life [2, 3]. Therefore, the complex relationship between the shock absorber condition and the on-ground dynamics of the aircraft makes the assessment of lateral stability a challenge in presence of component degradation.

Because of the problem complexity, the fundamental tools that have been extensively used to analyze aircraft on-ground dynamics are simulation environments aided by simple analytical models [4]. Several works have appeared that attempt to characterize the impact of specific system characteristics on lateral stability. In [5], a simple bicycle model was used to understand the impact of velocity and aerodynamic forces on the understeering gain. That work was later extended in [6] with improved 2-degree and 3-degree of freedom models to investigate the effect of tire inflation pressure and cornering stiffness on lateral stability. A similar approach was followed in [7] to evaluate the effect of aircraft weight and center of gravity position. A different approach was proposed in [8] in which a multibody simulation environment was coupled with a bifurcation analysis to assess lateral stability under different steering commands and thrust regimes. The previous approach was later complemented in [9] with an analytical 6-degrees of freedom model used to evaluate the effect of aircraft mass and center of gravity position on ground handling. In contrast, very limited work has been focused on assessing the impact of shock absorber leakage on aircraft ground handling. It is known that the health condition of the shock absorber impacts the handling capabilities of any ground vehicle [10]. Works from the automotive field such as [11] and [12] have pointed out the coupling between shock absorber stiffness, stability, and braking distances. Different studies have attempted to model shock absorber failure and variability in aircraft to analyze vertical dynamics [13], to propose anomaly detection schemes [2, 14], or to analyze vibration phenomena [15]. However, no analysis is provided in terms of the impact of shock absorber leakage on aircraft lateral stability.

This paper establishes links between the shock absorber gas leakage and the lateral stability properties of aircraft during on-ground operation in regimes common in braking maneuvers. The analysis is conducted in a MATLAB Simulink simulation environment, through the construction of a high-fidelity multibody representation of a typical tricycle landing gear trainer aircraft, which is validated against experimental data from a case study in collaboration with an industrial partner. Two analytical models are also developed to produce intuitive assessments on the shock absorber leakage on lateral stability.

The structure of the paper is as follows. Section II introduces the multibody simulation environment, describing all

of its fundamental blocks, operating modes, and providing the experimental validation results. Then, Sec. III introduces the analytical models that enable the analysis of the system in its different operating modes. Section IV presents the sensitivity analysis over different operating conditions, establishing the link between shock absorber leakage and lateral stability.
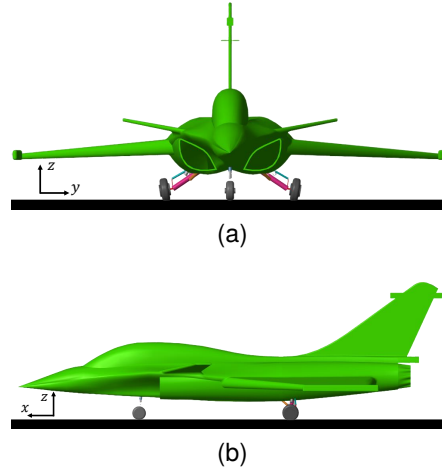
**Fig. 1    Aircraft Rigid Body Model geometry in the Multibody Simulator. Top: Front View. Bottom: Lateral View.**

## II. Multibody Simulation Environment

In this work, the system under consideration corresponds to a trainer aircraft endowed with a tricycle retractable landing gear, studied during its operation phases while ground contact is present. Significant efforts have been made in order to accurately model the landing gear geometrical and dynamical characteristics. The undercarriage present in the two rear wheels will be denoted as the Main Landing Gear (MLG), whereas the front wheel undercarriage will be denoted as the Nose Landing Gear (NLG). Each landing gear is composed of structural support elements, a shock absorber, and its corresponding wheel. The most important dynamical effects encountered during a braking maneuver have been included in the model, such as landing gear track variation, surface friction characteristics, lift and drag aerodynamic forces, and braking actuator dynamics. The noise level was estimated from measurement samples obtained from the same sensors installed in the real system. In addition, two different operating modes are implemented depending on the presence or absence of NLG wheel steering capability, which leads to different dynamics. The system as a whole is interesting due to its high level of complexity, and also because of the existing coupling between the longitudinal and the lateral dynamics induced by the MLG geometry. The simulation environment used within this work is implemented through the framework provided by the MATLAB Simulink Simscape Multibody library [16], which enables the construction of complex geometries through the definition of rigid bodies, joints, and suitable inertial and geometrical constraints. The interactions between bodies are highly adaptable and allow for the definition of custom implementations of contact forces, friction laws or damping profiles, through the usage of the functionalities provided by the Simulink modeling framework. In the following subsections, the different elements composing the system are described.
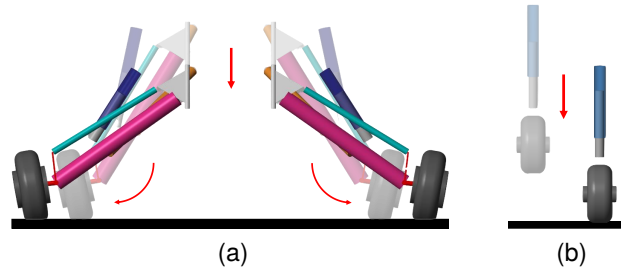
**Fig. 2   Landing Gear Geometry. Left: Main Landing Gear unloaded (light silhouette) and loaded (solid figure). Right: Nose Landing Gear unloaded (light silhouette) and loaded (solid figure).**
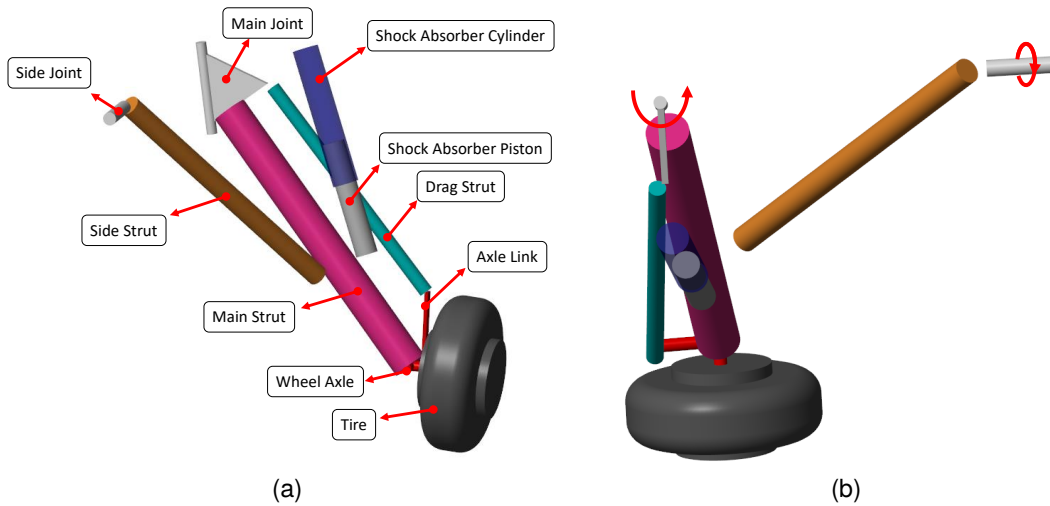


**Fig. 3   Main Landing Gear Geometry. Left: The main rigid bodies and joints composing the structure are shown. Right: Top view highlighting the degrees of freedom provided by the Main Joint and Side Joint.**

## A. Aircraft and Landing Gear Geometry

The aircraft model geometry in the simulation environment is presented in Fig. 1. The geometrical characteristics as well as its inertial parameters have been extracted from official blueprints from the industrial partner providing the experimental data for the model construction. The main aircraft body is represented by a single rigid body component with a center of gravity in a location depending on the selected payload configuration. The aircraft body shown in green in Fig. 1 is meant as a representative geometry of a trainer aircraft and how its integration in the multibody simulation environment would look like. As such, it should not be considered as the body geometry of the actual aircraft under study.

As can be appreciated in Fig. 1, the aircraft body is supported by the MLG at the rear, and by the NLG at the front. A detail of the MLG and NLG is depicted in Fig. 2. As shown by Fig. 2a, a series of rigid bodies connected by spherical joints implement the kinematic constraints present in the real landing gear, allowing the gear track length to extend or shrink depending on the weight sustained by the mechanism. In contrast, as appreciated from Fig. 2b, only the most elemental components have been retained while modeling the NLG geometry, as most of the structural elements are

intended to provide steering capability to the front wheel, which is included in the multibody model by a rotational joint.

A further detailed view of the MLG is provided in Fig. 3a. The MLG is attached to the fuselage by the Main Joint, the Side Joint, the Shock Absorber, and the Drag Strut. As shown in Fig. 3b, the Main Joint and Side Joint enable the rotation of the MLG around their main axes, allowing the motion of the whole structure relative to the fuselage. The Side Strut provides structural support by distributing the load sustained by the mechanism. The Shock Absorber is composed by a piston connected to the Main Strut that is allowed to move inside the cylinder, connected in turn to the fuselage. The Drag Strut, connected to the fuselage and to the Axle Link, limits the orientation of the Wheel Axle.

**B. System Operating Modes**

Within the simulation framework constructed, and similarly to the real system under study, two inputs can be used to control the lateral dynamics. On one hand, there is a braking actuator on each wheel of the MLG, able to provide a braking torque, and mainly used to bring the aircraft to standstill. In contrast, the NLG has no braking actuators available to the pilot. On the other hand, a steering actuator may be available to turn the front wheel at the NLG at the request of the pilot. Conversely, the MLG wheels have no steering capability. In this work, two modes of operation will be analyzed:

1) **Engaged Steering Mode:** In this scenario, the front NLG wheel steering is enabled, so that the pilot can generate a steering angle $\delta_f$ by moving the steering wheel inside the cockpit. For the scope of the present study, the steering angle $\delta_f$ has been considered as the effective steering angle generated at the NLG instead of the steering angle command requested by the pilot. The previous definition implies that the nose wheel steering actuator dynamics have not being considered.

   In this mode, the braking actuators on both wheels are also activated, so that by using the corresponding pedals, the pilot can generate a braking torque $T_b$ on each wheel, through a hydraulic system that enables to push a caliper against a set of disc brakes.

2) **Differential Braking Mode:** In this case, the front NLG wheel steering is disabled, so that the pilot does not impose the steering angle $\delta$. Instead, the pilot only operates the braking actuators on both wheels. This means that the nose wheel is free to rotate, and the steering angle $\delta$ becomes an output of the system as well. The steering angle $\delta$ evolves according to its own dynamics, determined by the inertial characteristics of the wheel, as well as the geometrical and dynamic parameters of the rotational joint at the NLG. The NLG is also endowed with a trailing arm, which causes a misalignment between its rotation axis and the wheel vertical axis, quantified by a distance parameter $d$. The implications of the trailing arm geometry on the lateral dynamics are analyzed in Section III.B.

With reference to the case study, the two modes of operation previously described correspond to different actuation usage profiles during a conventional ground handling maneuver. In general, the most commonly employed steering
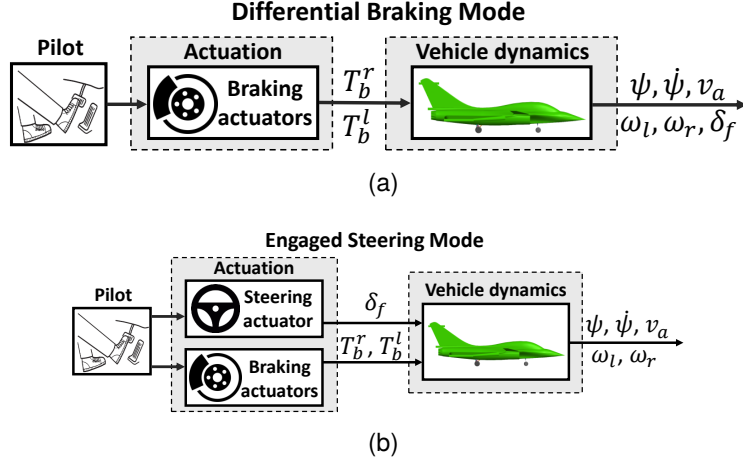
**Fig. 4 Schematic view of the operation modes available in the Multibody Simulator, along with their associated dynamic variables. Top: Engaged Steering Mode. Bottom: Differential Braking Mode.**

method for the considered aircraft is the Differential Braking Mode. As such, in case sufficient steering capability is provided by using the MLG braking actuators, the maneuver is completed without using the nose wheel steering. In contrast, if the pilot judges that increased steering authority is required to safely complete a maneuver, the steering capability of the nose wheel will be exploited and the aircraft operation will transition to the Engaged Steering Mode.

A simple illustration of the implemented operation modes is shown in Fig. 4. As can be noticed, in the Engaged Steering Mode, the combined action of the steering angle $\delta$ and braking torques at the right ($T_b^r$) and left ($T_b^l$) wheels will determine the dynamic evolution of the aircraft body velocity $v_a$, the wheel speeds at the right ($\omega_r$) and left ($\omega_l$) sides of the MLG, the yaw rate $\dot{\psi}$ and the yaw $\psi$. Instead, in the Differential Braking Mode, the aircraft dynamics are controlled only via the braking torques $T_b^r$ and $T_b^l$, with the steering angle $\delta$ representing one of the output variables.

### C. Tire-Runway and External Forces Interaction Model

For the development of the model, it is assumed that the operational envelope of the system under study rules out the possibility of side landings or aerodynamic phenomena such as wind gusts that overly excite the lateral dynamics. It is also assumed that the analyzed longitudinal aircraft velocity reaches up to 120 [km/h], which corresponds to the second half of a conventional landing or Rejected Take-Off (RTO) maneuver for the case study. The previous considerations allow to neglect the effects of aerodynamic lateral forces, as well as yaw and pitching moments, which remain limited in comparison to the tire-runway contact forces.

The wheels on both the MLG and NLG are implemented by means of solid bodies with corresponding masses, geometries and inertial characteristics as provided by the manufacturer. To capture the exchange of forces that happens between the tires and the surface of the ground, the usual decomposition in three components is adopted: the longitudinal force $F_x$, the lateral force $F_y$ and the vertical force $F_z$. For each tire, the first two forces can be described by a functional

relationship of the following form:

$$F_x = F_x \left( F_z^w, \alpha, \lambda \right) \tag{1a}$$

$$F_y = F_y \left( F_z^w, \alpha, \lambda \right) \tag{1b}$$

where $F_z^w$ describes the equivalent vertical load experienced by the tire; $\alpha$ is the side-slip angle, defined as the angle between the velocity vector of the contact point with respect to the tire longitudinal axis; and $\lambda$, which is the longitudinal wheel slip. In turn, the vertical load $F_z^w$ is computed by means of a linear contact dynamic in which the wheel is allowed to penetrate the runway surface as follows:

$$F_z^w = K_c \delta_z + C_c \dot{\delta}_z \tag{2}$$

where $\delta_z$ and $\dot{\delta}_z$ are the penetration displacement and velocity between the runway and the wheel, respectively; whereas $K_c$ and $C_c$ are their corresponding stiffness and damping parameters, which have been extracted from experimental data by analyzing results from wheel drop tests and deflection curves provided by the industrial partner. The penetration displacement $\delta_z$ and penetration velocity $\dot{\delta}_z$ will be influenced by the aircraft mass $m_a$ and aerodynamic lift force, which together determine a velocity-dependent aircraft main body vertical load $F_z(v_a)$. Its expression will read:

$$F_z(v_a) = m_a g - \frac{1}{2} \rho v_a^2 S C_L \tag{3}$$

where $g$ is the gravity acceleration, $\rho$ is the air mass density, $v_a$ is the longitudinal speed of the aircraft, $S$ is the reference area, and $C_L$ is the lift coefficient. The lift coefficient data has been provided by the industrial partner, based on internal models. Next, the longitudinal wheel slip $\lambda$ for a braking maneuver is defined as:

$$\lambda = \frac{v_a - \omega r \cos \alpha}{v_a} \tag{4}$$

where $\omega$ is the rotational wheel speed and $r$ is the radius of the wheel. As expressed by Eq. (4), $\lambda \in [0, 1]$, with $\lambda = 0$ representing the free-rolling condition and $\lambda = 1$ the locked-wheel condition. The side-slip angle $\alpha$ is obtained as:

$$\alpha = \arctan \left( \frac{V_y^w}{V_x^w} \right) \tag{5}$$

where $V_x^w$ and $V_y^w$ are the longitudinal and lateral wheel velocities along the local wheel reference frame.

The contact forces between the wheels and the runway were implemented using the Simscape Multibody Contact Forces Library [16], and calculating the longitudinal and lateral forces in Eqs. (1a) and (1b) by the Fiala Model [17]. This model belongs to the class of nonlinear analytical tire models that were developed as an extension of the brush
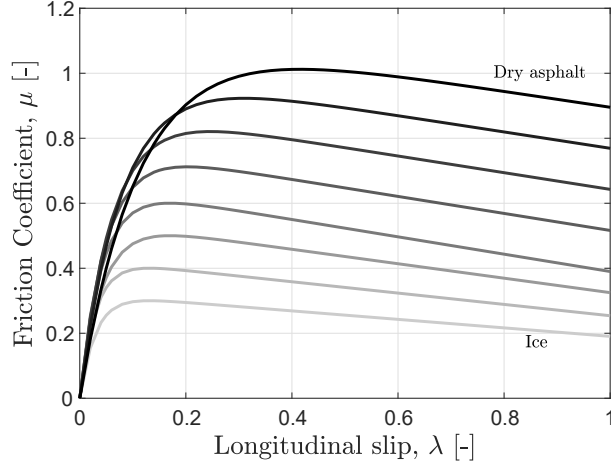
**Fig. 5   Burckhardt friction model. The eight represented curves allow conditions ranging from wet/slippery surfaces (bottom curves) to dry/high-grip surfaces (top curves).**

model, by considering a parabolic carcass deflection. Additional details of the model can be consulted in [18]. The main parameters required for its implementation are the characteristics of the longitudinal and lateral stiffness of the tire being employed. For the present work, these values have been provided by the industrial partner. Note that the wheel camber angle contribution has been neglected in the force exchange calculation due to the limited values it assumes during a braking maneuver.

The longitudinal friction coefficient $\mu$ between the ground and the tire has been characterized by the widely used Burckhardt model [19]. The analytical relationship is expressed as follows:

$$\mu(\lambda) = \theta_1 \left(1 - e^{-\lambda\theta_2}\right) - \lambda\theta_3 \tag{6}$$

where $\theta_1$, $\theta_2$ and $\theta_3$ are parameters characteristic of the runway condition. For this work, eight different friction conditions will be employed, identified from experimental data. For reasons of confidentiality, the exact parameters $\theta_1$, $\theta_2$ and $\theta_3$ cannot be supplied, but the graphical representation of the curves is given in Fig. 5. In addition, a frontal aerodynamic drag force is considered, affecting the longitudinal dynamics. Its expression is considered as:

$$F_{drag}(v_a) = \frac{1}{2}\rho v_a^2 S C_D \tag{7}$$

with $C_D$ the drag coefficient, extracted from experimental data.

### D. Braking Actuator Model

Both sides of the MLG have the capability to provide braking torque to each corresponding wheel to bring the aircraft to standstill. In contrast, the NLG lacks such capability. The system under study employs electro-hydraulic
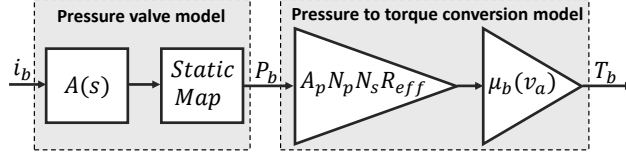
**Fig. 6 Schematic representation of the actuator model: from the input braking current $i_b$ to the output braking torque $T_b$.**
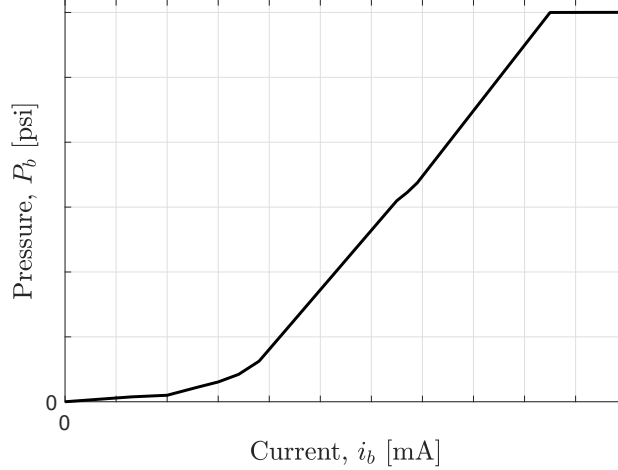


**Fig. 7 Nonlinear static map between current $i_b$ and pressure $P_b$.**

servo valves to generate the braking torque. To do so, an input current $i_b$ is fed to the actuator and converted into a certain pressure $P_b$ generated by the hydraulic system. The pressure is then employed to push a caliper against the disc brake rotor, and friction is generated between the brake pad attached to the caliper and the disc itself, providing an output torque $T_b$. The full actuator model is presented in Fig. 6. To describe the conversion between current $i_b$ and pressure $P_b$, denoted as Pressure valve model in Fig. 6, a linear second-order dynamic model with delay has been experimentally obtained, in conjunction with a nonlinear static gain depending on the operating region of the system. The dynamic part of the current to pressure relationship is captured by the following expression:

$$A(s) = \frac{e^{-\tau s}}{\left(1 + \frac{2\xi s}{\omega_n} + \frac{s^2}{\omega_n^2}\right)} \tag{8}$$

with $\tau$ being the actuator delay due to the fluid transfer, $\xi$ the damping coefficient, and $\omega_n$ the natural frequency. The parameters required in Eq. (8) have been experimentally identified by conventional system identification techniques employing different current excitations. The nonlinear static map is presented in Fig. 7, where three distinct regions can be appreciated: a startup zone, a linear zone, and a saturation zone. Further details about the experimental set-up and associated results are provided in [20].

Once the pressure $P_b$ is obtained, the braking torque $T_b$ is computed through a series of gains, denoted as Pressure to

## Table 2   Braking Maneuver Data

| CONFIG | mass kg | initial speed m/s |
|---|---|---|
| Light landing | 2800 | 49 |
| Medium landing (a) | 3150 | 52 |
| Medium landing (b) | 3300 | 53 |
| Heavy landing | 4450 | 61 |

torque conversion model in Fig. 6. The first set of gains capture the static portion of the conversion, which are obtained from the actuator physical parameters. As illustrated in Fig. 6, the factors include: the braking pads surface area $A_p$, the number of pistons $N_p$, the number of braking pads per piston $N_s$, and the effective radius of the contact point of the sliding surfaces $R_{eff}$. Finally, the last gain models the nonlinear dynamic variation of the friction coefficient $\mu_b$ within each single braking maneuver, and which is induced by the overheating process acting on the actuator components, see [21, 22].

Different approaches have been presented in the literature in order to capture the evolution of the brake pad friction coefficient. One of the most well known models is the Ostermeyer model, which employs a two-state dynamical system dependent on the local braking pad temperature [23]. Most recently, attempts have been made to derive data-driven models of this phenomenon [24], at least in the automotive context. To preserve modeling simplicity, a common approach employed to account for such behavior is to identify a proxy variable that correlates with the variation in $\mu_b$, see [21, 25]. In this work, the aircraft longitudinal speed $v_a$ has been chosen for that purpose, as experimental measurements in different system configurations were available as part of the braking actuator characterization campaign. In particular, the dynamic friction coefficient behavior was captured in four different speed regimes, consistent with standardized braking maneuvers for the application at hand, with different aircraft payload configurations. The characteristics of the considered landing maneuvers are presented in Table 2. The measured evolution of the friction coefficient with respect to the longitudinal aircraft speed followed three different trends, each of which is presented in Table 2 and in Fig. 8, in which the experimental data are overlaid with the fitted curves used in the simulator for implementing the friction coefficient dynamics. As can be appreciated, the load has a considerable impact on the dynamic braking coefficient evolution.

### E. Shock Absorber and Leakage Model

Each structural component assembly of the MLG and NLG is equipped with an oleo-pneumatic shock absorber, connected between the wheel support and the air-frame underside. The system under study employs two telescopic cylinders, the upper one fixed to the aircraft fuselage, whereas the lower one is allowed to move vertically while attached to the wheel support assembly. By construction, two chambers are defined, the lower one filled with hydraulic fluid, while the upper one is filled with compressed gas. To represent the forces generated inside the component during
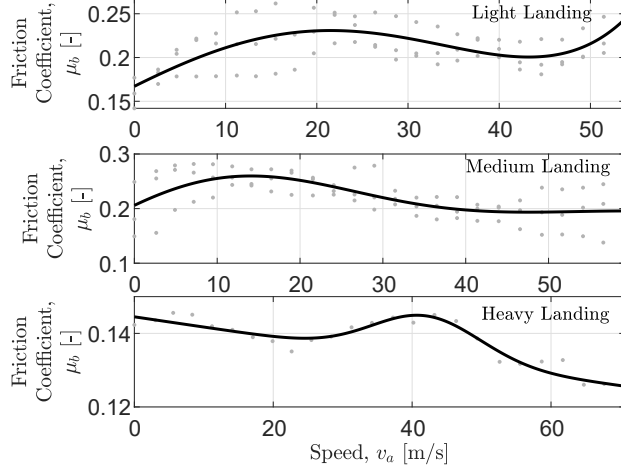
**Fig. 8  Dynamic evolution of the friction coefficient during a standard maneuver. Top: Light Landing maneuver. Middle: Medium Landing maneuvers. Bottom: Heavy Landing maneuver.**

the compression or extension of the shock absorber, a nonlinear polytropic compression law is used, coupled with a velocity-squared damping, as in [26, 27]. In particular, a pneumatic force $F_e$ is generated due to the compression of the gas in the upper chamber of the assembly that can be described by a polytropic law of the following form:

$$F_e(s) = p_0 A \left( \frac{V_0}{V_0 - As} \right)^n \tag{9}$$

where $p_0$ is the air pressure at the upper chamber at fully extended condition, $V_0$ is the air volume of the upper chamber at fully extended condition, $A$ is the constant cross-sectional area of the chamber, $s$ is the shock absorber stroke, and $n$ is the polytropic coefficient. As can be seen from Eq. (9), this force is a highly nonlinear function of the stroke $s$ of the shock absorber. The so-called preload force of the shock absorber is attained when $s = 0$. The particular parameters required to describe the corresponding load-stroke profile arising from Eq. (9) have been obtained from manufacturer data at nominal conditions, and the resultant curves are exposed in Fig. 9 for both the MLG and NLG. In Fig. 9, also some stroke values are highlighted that indicate the variation in the static equilibrium position induced by the MLG leakage. The vertical axes values have been removed for confidentiality reasons. The previous consideration applies for all subsequent graphs lacking the vertical axes values in this paper, which consist of data provided by a component manufacturer or obtained from experimental tests.

In turn, a hydraulic force $F_h$ results from the resistance of the fluid to flow from the lower chamber to the upper chamber through the small orifice in the interface between the two compartments. The expression of such force will assume the following form:

$$F_h(s, \dot{s}) = \frac{\rho_h A_h^3}{2(c_d A_n(s))^2} \dot{s}^2 \, \text{sign}(\dot{s}) \tag{10}$$

where $\dot{s}$ is the stroke speed, $\rho_h$ is the mass density of the hydraulic fluid, $A_h$ is the hydraulic plate area, $c_d$ is the
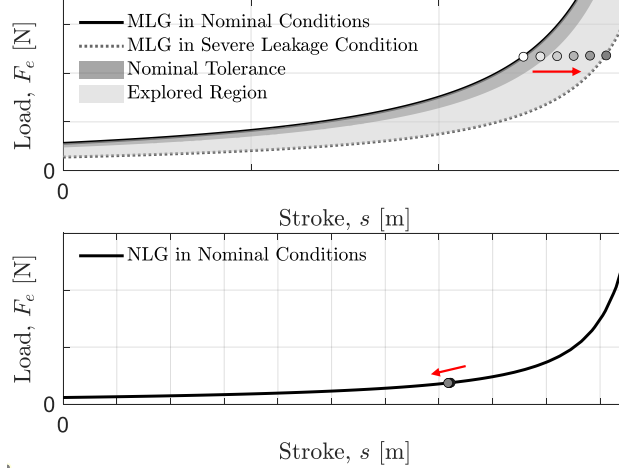
15

**Fig. 9** Top: MLG shock absorber load-stroke profile with the analyzed operating ranges of the component. Bottom: NLG shock absorber load-stroke nominal profile. Circular markers are superimposed to indicate the variation in stroke for a Heavy Landing scenario in different leakage conditions. The arrow points towards an increasing MLG leakage condition.

discharge coefficient, and $A_n(s)$ is the net orifice area. The dependence of the orifice area on the stroke position reflects the fact that a metering pin with varying cross-sectional area is employed. In this manner, the first set of factors in Eq. (10) can be collapsed into a coefficient $c(s)$. The final expression then will read:

$$F_h(s, \dot{s}) = c(s)\dot{s}^2 \operatorname{sign}(\dot{s}) \tag{11}$$

Both the MLG and NLG associated $c(s)$ coefficients have been extracted from manufacturer data, and their associated curves are presented in Fig. 10. As can be appreciated, the friction coefficient has a strong stroke-dependent characteristic, and a different profile depending on the stroke velocity direction. The varying cross-sectional area of the orifice with the stroke position, as well as the design of the fluid return path are contributing factors to the shape of the curves in Fig. 10. In general, the curves are shaped to obtain desirable damping characteristics to dissipate the vertical kinetic energy upon landing.

One of the most common faults affecting oleo-pneumatic shock absorbers is having an incorrect amount of oil or gas in the chambers of the assembly [3]. In particular, gas and/or oil leakage will worsen the performance of the shock absorber, altering its dynamic characteristics and risking an insufficient capacity to dissipate the high amounts of kinetic energy sustained during landing. In case a linear elastic and damping law is considered, a scaling of the associated coefficients can be applied to model these kinds of faults, as done in [28]. However, even in the case of nonlinear force-stroke characteristics, the full pneumatic force curve can be shifted to represent the leakage phenomenon, as done in [14]. The two approaches can be linked by analyzing the linearization of the profile to obtain an equivalent stiffness, as done in [2].
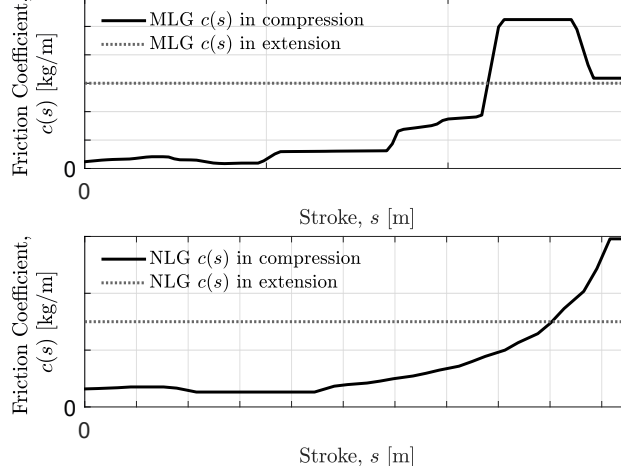
**Fig. 10   Hydraulic force $F_h$ nonlinear stroke-dependent coefficient $c(s)$. Top: MLG case. Bottom: NLG case.**

This work considers asymmetrical gas leakages located at the MLG shock absorbers, which sustain most of the weight of the aircraft during landing. The previous assumption implies that one of the two MLG shock absorbers is left in nominal conditions, while different levels of gas leakage are considered for the other MLG shock absorber. Without loss of generality, the faulty shock absorber will be the one present at the right MLG. In order to model gas leakages, a scaling of the MLG pneumatic force nonlinear curve is considered, in which it is assumed that the geometrical characteristics of the shock absorber are preserved, so that the fully extended volume $V_0$ and the cross-sectional area $A$ are constant. It is also assumed that the polytropic coefficient $n$ is not altered. Instead, the pressure $p_0$ at fully extended condition is altered due to the change in relative quantities between the oil and gas at equilibrium. Intuitively, this change, as shown by Eq. (9), corresponds to a scaling in the preload force. Experimental tests revealed that for the case study there exists a certain acceptable range of shock absorber preload variation up to which the component can be inside the nominal tolerance, amounting to a 15% reduction of the preload factor, as illustrated in Fig. 9. Further reductions of the preload factor can be considered effectively as a leakage condition.

**F. Simulation Environment Validation**

The defined simulation framework has been validated in a series of braking maneuver scenarios enabling to check the correspondence of the main predicted quantities against available experimental data, which were collected with the MLG shock absorbers in a nominal condition. Some representative braking maneuvers will be presented, by initializing the simulation model with the same aircraft inertial configuration, as well as the same initial aircraft velocity $v_a$ that was recorded in the experimental tests, and then feeding in open loop the corresponding experimental actuator signals. In what follows, both operating modes will be discussed.
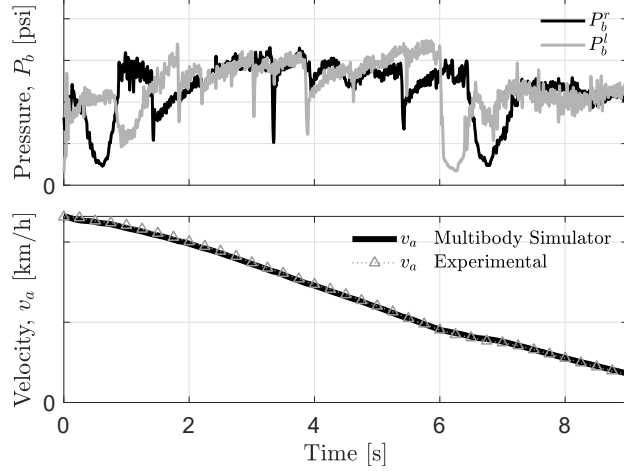
17

**Fig. 11  Comparison between the experimental and simulated velocity profile for an RTO maneuver. Top: Applied pressures on the braking actuators of the MLG. Bottom: Longitudinal aircraft velocity.**
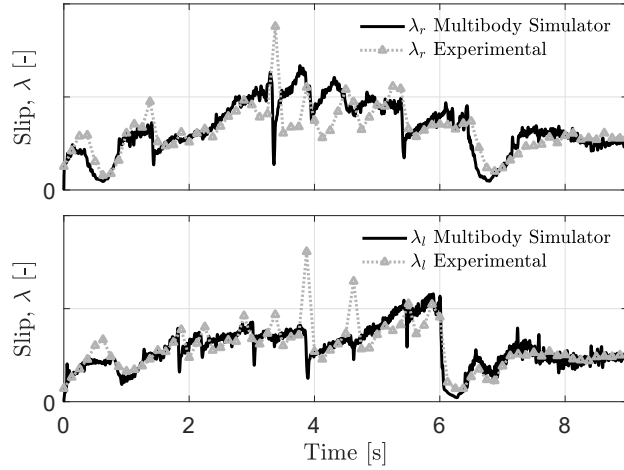


**Fig. 12  Comparison between the experimental and simulated slip $\lambda$ on both MLG sides for an RTO maneuver. Top: Right MLG. Bottom: Left MLG.**

*1. Engaged Steering Mode*

The first considered scenario is a Rejected-Take Off (RTO) braking maneuver, with an initial speed of around 110 km/h. The steering wheel was fixed to a null input, while the braking pressures applied on each side of the MLG were largely similar. In order to generate such pressure profiles, the pilot was tasked with applying the braking pedals in a symmetrical manner for the duration of the maneuver. To ensure the generated pressure profiles were safe for the pilot, the anti-skid system was left active. The rudder was not actuated during the maneuver. Moreover, to have a realistic description of the thrust forces during this type of maneuver, a standard RTO thrust curve provided by the industrial partner was used, which describes the thrust forces as a function of the longitudinal aircraft velocity.

In this manner, the aircraft traced a straight path along the runway, which allows to verify the simulation model longitudinal braking dynamics. The results of such test are presented in Fig. 11 and Fig. 12.  In Fig. 11, the top plot

18

highlights the applied input pressures $P_b^r$ and $P_b^l$ on both sides of the MLG. The bottom plot shows the comparison between the resultant experimental and simulated aircraft velocity profiles $v_a$. Finally, the two plots in Fig. 12 show the comparison between the experimental and simulated longitudinal slips $\lambda_l$ and $\lambda_r$ for the left and right sides of the MLG.

From the graphs in Fig. 12, it can be noticed that a slight asymmetric behavior is present between the evolution of the longitudinal slip signals. The previous point can be mostly explained by the asymmetries observed in the pressure profiles applied to the system, exposed in Fig. 11. In turn, most of the asymmetries in the generated pressure profiles can be attributed to 2 factors. On one hand, the pedal application by the pilot was not completely symmetric, and produced pressure requests to the braking system which were not exactly the same for both MLG sides. On the other hand, during the characterization of the braking system, an imperfect match between the braking actuators in the right and left sides of the MLG was often observed. In this manner, the braking actuator condition can also impact the pressure profile generation. The previous point means that the current-to-pressure and the pressure-to-torque relationship between the braking actuators may not have been necessarily the same, and it is possible some variability was introduced through that mechanism on the conducted experiment.

It can also be appreciated from Fig. 12 that some longitudinal slip peaks, especially some high amplitude peaks, evolve in opposite directions between the experimental and the multibody simulator. This point can be attributed to a suboptimal description of the wheel slip dynamics near the peak of the friction curve, typically difficult to represent. As the anti-skid system aims to maximize braking performance by constantly trying to enter the wheel slip instability region, high-frequency events of high amplitude slip peaks occur, as the wheel slip is corrected by the anti-skid system by quickly reducing the applied braking pressure. The developed model misses some of the described events, capturing instead the reduction in wheel slip induced by the braking pressure reduction. In any case, the match between both the experimental and the simulated dynamics is evident, and allows to confirm the adequate quality of the longitudinal braking dynamics model prediction.

The second scenario considers a maneuver in which the braking actuator was not applied, but the steering wheel at the NLG was actuated, at an aircraft velocity of around 100 km/h. This allows to generate a non-zero steering angle $\delta_f$ to purposely excite the lateral system dynamics. The rudder was not actuated during the maneuver. In this case, the representation of the thrust forces was treated by using a standard landing thrust curve provided by the industrial partner, which also describes the thrust forces as a function of the longitudinal aircraft velocity.

The main involved quantities arising from such situation are the yaw rate $\dot{\psi}$, the aircraft side-slip angle $\beta$, the lateral acceleration $a_y$, the lateral velocity $V_y$, and the front wheel side-slip angle $\alpha_f$ with respect to the front wheel velocity vector $v_f$. The relevant quantities are graphically illustrated in Fig. 13.

In this case, the applied input generated an oscillatory movement of the aircraft about the runway centerline, allowing to verify the simulation model lateral dynamics. The results of the test can be appreciated in Fig. 14 and Fig. 15. As can be observed, the obtained match between the simulation and the experimental data is satisfactory for all the
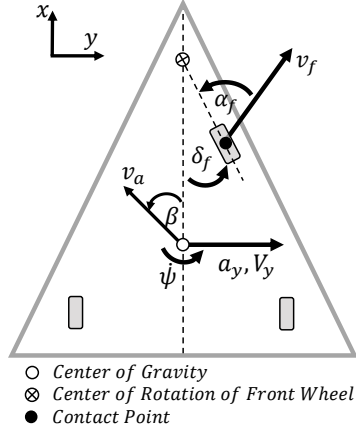
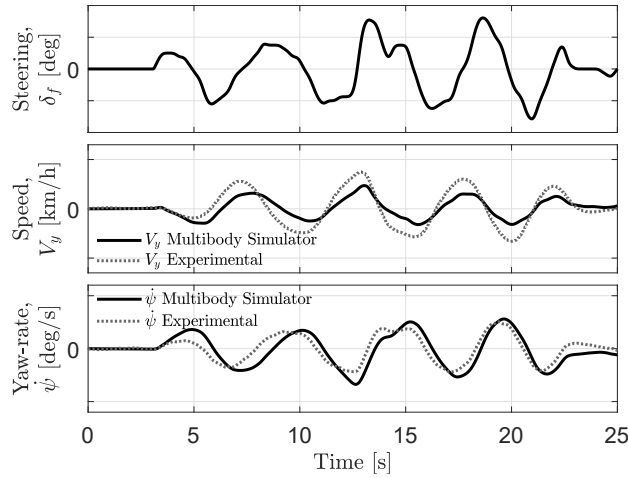**Fig. 13 Conceptual representation of the main quantities involved in the lateral aircraft dynamics.**



**Fig. 14 Comparison between the experimental and simulated quantities of the lateral dynamics for a steering input maneuver. Top: Steering input $\delta_f$. Middle: Lateral velocity $V_y$. Bottom: Yaw rate $\dot{\psi}$.**

monitored quantities regarding the lateral dynamics. Both the amplitude and the phases of the profiles are in the expected ranges, with an adequate resemblance also on the waveforms in each of the analyzed variables.

*2. Differential Braking Mode*

For the evaluation of the Differential Braking Mode lateral dynamics, the third scenario considers a maneuver in which the braking actuators from the MLG were applied in an asymmetric manner, at an aircraft velocity of around 130 km/h. The same quantities highlighted in Fig. 13 are of interest. In this case, the input fed to the system considers the recorded experimental pressures $P_b^r$ and $P_b^l$. The rudder was not actuated during the maneuver. The representation of the thrust forces was treated by using the same standard landing thrust curve provided by the industrial partner as in the second scenario from the Engaged Steering Mode.

For brevity of exposition, the results for the most relevant system states are reported in Fig. 16, where the asymmetric
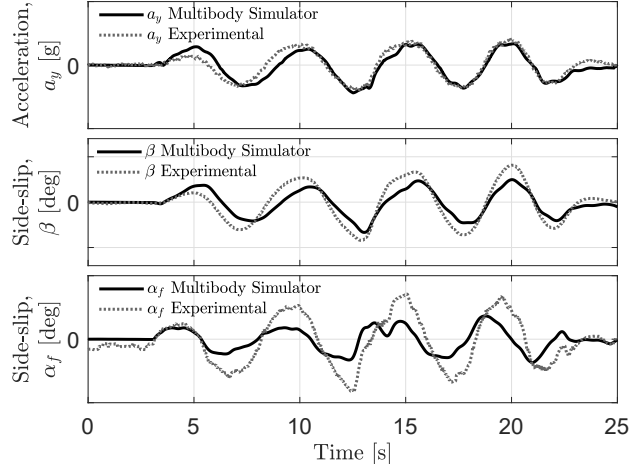
**Fig. 15 Comparison between the experimental and simulated quantities of the lateral dynamics for a steering input maneuver. Top: Lateral acceleration $a_y$. Middle: Aircraft body side-slip angle $\beta$. Bottom: Front side-slip angle $\alpha_f$.**

applied pressures are detailed, as well as the obtained steering angle $\delta_f$, lateral velocity $V_y$, and yaw rate $\dot{\psi}$. As can be appreciated, the simulator exhibits in general the same dynamics as the experimental data. The main difference can be observed in the lateral velocity $V_y$ evolution, in which the simulator waveform lags behind the experimental data after the excitation pressure is removed towards the end of the maneuver. The difference can be explained due to the steering damping $c_s$ that had to be chosen in the steering rotational joint of the Multibody Simulator, for which no manufacturer data was available. Hence, the best compromise possible was chosen between the fitting quality of the steering $\delta_f$, and lateral dynamic quantities such as the lateral velocity $V_y$. Nevertheless, the simulation model still shows an adequate capability in predicting the lateral system dynamics also for the Differential Braking Mode.
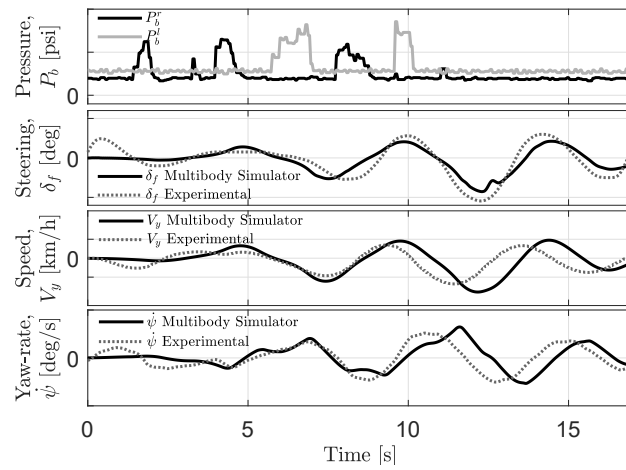
**Fig. 16    Comparison between the experimental and simulated quantities of the lateral dynamics for a differential braking maneuver. First Plot: Applied pressures $P_b^r$ and $P_b^l$. Second Plot: Steering angle $\delta_f$. Third Plot: Lateral velocity $V_y$. Fourth Plot: Yaw rate $\dot{\psi}$.**

# III. Simplified Analytical Models

In this section, two analytical models describing the aircraft lateral dynamics are presented, each one associated to an operating mode of the aircraft under study. The defined models should be complex enough to capture the dominant lateral system dynamics in the corresponding operating condition, and sufficiently simple to allow for meaningful conclusions to be drawn. By linking the impact of the MLG shock absorber leakage on the complex Multibody Simulator defined in Sec. II, with changes in key parameters and system properties from the simplified analytical models, an assessment can be made about the lateral stability properties of the aircraft. This procedure allows to quantify the impact of the MLG shock absorber leakage in terms of commonly employed stability metrics.

Even though the proposed analytical models are employed in this work to characterize the shock absorber leakage impact on lateral aircraft stability, their usefulness can go beyond the realm of analysis. Model-based control system design practice can also benefit from the availability of simple analytical models with parameters linked to physical phenomena. The availability of such models can allow the designer to theoretically investigate control and estimation laws and obtain parameter-dependent results, such as guarantees on system robustness. Therefore, the developed models are also to be seen as a step towards the design of robust controllers for lateral aircraft stability, which is a topic of ongoing work by the authors.

The following subsections are devoted to the description of such analytical models of the lateral dynamics.

## A. Bicycle Model

To characterize the Engaged Steering Mode, the simplest and most widely used model for the characterization of lateral vehicle dynamics will be employed, known as the Bicycle Model [29]. This model squashes the vehicle into a single track, consisting of two wheels, with the front one able to provide a steering angle $\delta_f$. A schematic representation of the model is depicted in Fig. 17. With reference to Fig. 17, the meaning of the variables involved in the model is as follows: $\dot{\psi}$ denotes the yaw rate of the vehicle; $F_{yr}$ and $F_{yf}$ are the rear and front lateral forces, respectively; $\delta_f$ is the steering angle of the front wheel, measured from the vehicle longitudinal axis to that of the front wheel; $\delta_r$ is a disturbance steering angle acting on the rear wheel; $\alpha_r$ and $\alpha_f$ are the rear and front side-slip angles, respectively; $v_r$ and $v_f$ are the rear and front velocity vectors of the rear and front wheels at the contact point, respectively; $v_a$ is the aircraft velocity vector; $\beta$ is the aircraft body side-slip angle; $l_r$ and $l_f$ are the distances from the rear and front wheel to the center of mass of the aircraft, respectively; and $L$ is the so-called vehicle wheelbase.

The model definition rests upon a set of simplifying assumptions. Small steering angles $\delta_f$ and $\delta_r$, as well as small side-slip angles $\alpha_r$, $\alpha_f$ and $\beta$ are assumed. In practice, this means that the maneuver turning radius is large, and the wheels are far from a full slip condition. In addition, a constant longitudinal velocity is considered. Furthermore, aerodynamic effects are also neglected. Even in the presence of all the previous simplifications, the Bicycle Model retains enough descriptive capability to be routinely employed in lateral vehicle dynamics analysis, particularly in the
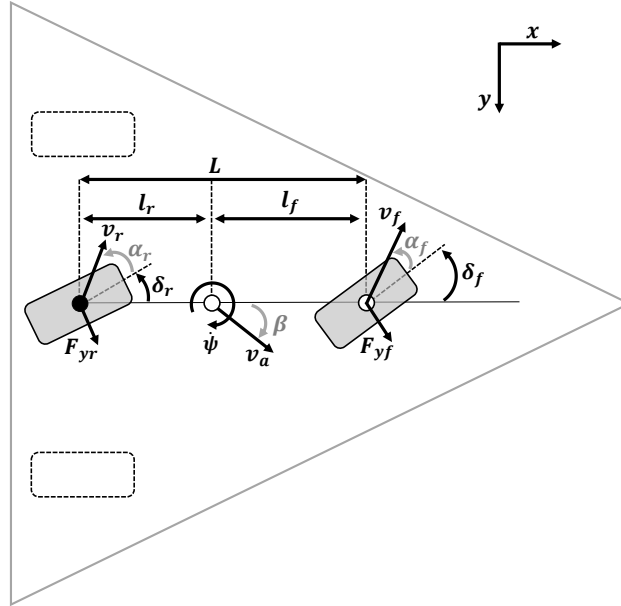
**Fig. 17    Conceptual representation of an aircraft bicycle model. The original position of the rear wheels is shown with dotted lines, whereas the positions of the wheels in the model are shown in solid grey.**

automotive field [30]. The most significant differences between the automotive and aeronautical contexts regarding the assumptions of this model lie in the operating velocity ranges and the significance of the aerodynamic forces. Aircraft braking maneuvers are usually performed at considerably higher speeds than their automotive counterparts. In these speed regimes, aircraft are affected by significant aerodynamic forces, out of which the lift and drag forces will provoke an impact in the longitudinal and vertical system dynamics. In this manner, neglecting the aerodynamic effects can still be considered as a reasonable simplification in low operating speeds. These regimes are still of significance for Rejected Take-Off maneuvers and the final portion of a landing braking maneuver. Nevertheless, the Bicycle Model has still been employed with success to analyze lateral aircraft dynamics [5].

The motivation for the addition of a rear wheel steering disturbance $\delta_r$ in the model is to provide a simple disturbance channel able to capture the effect of an asymmetrical shock absorber gas leakage in the lateral aircraft dynamics. As shown in Fig. 9, an MLG shock absorber leakage will alter the static equilibrium of the system, inducing an additional compression in the shock absorber subject to the leakage. In turn, the induced asymmetry between both MLG sides may get coupled with the compliance of the MLG to lateral motions, particularly the one provided by the Main Joint degree of freedom shown in Fig. 3b.

The dynamic equations involved in the model can be obtained by performing a lateral force and moment balance,

yielding the following system:

$$m_a v_a (\dot{\beta} + \dot{\psi}) = F_{yf} + F_{yr} \tag{12a}$$

$$J_G \ddot{\psi} = F_{yf} l_f - F_{yr} l_r \tag{12b}$$

where $J_G$ is the moment of inertia of the aircraft around the vertical axis passing through the center of gravity. It is possible to find the front and rear side-slip angles $\alpha_f$ and $\alpha_r$ as a function of the other involved dynamic quantities. The expressions will read:

$$\alpha_f = \frac{v_a \beta + l_f \dot{\psi}}{v_a} - \delta_f \tag{13a}$$

$$\alpha_r = \frac{v_a \beta - l_r \dot{\psi}}{v_a} - \delta_r \tag{13b}$$

The final dynamic model can be obtained by the introduction of the lateral cornering-stiffness for the front and rear wheels $C_f$ and $C_r$, which are the slopes of the lateral force $F_y$-slip $\alpha$ curve. Normally, the curve exhibits a nonlinear characteristic, but keeping the slip angles small, the following relations hold:

$$F_{yr} = C_r \alpha_r \tag{14a}$$

$$F_{yf} = C_f \alpha_f \tag{14b}$$

In this manner, combining Eqs. (12), (13) and (14), considering the aircraft body side-slip angle $\beta$ and the yaw rate $\dot{\psi}$ as states $x$ and outputs $y$, by proposing the front steering angle $\delta_f$ as an input $u$, and by proposing the rear steering angle $\delta_r$ as a disturbance $d_\delta$, the following state-space model can be obtained:

$$\dot{x} = \begin{bmatrix} \dot{\beta} \\ \ddot{\psi} \end{bmatrix} = \begin{bmatrix} -\frac{C_r + C_f}{m_a v_a} & -1 + \frac{C_r l_r - C_f l_f}{m_a v_a^2} \\ \frac{C_r l_r - C_f l_f}{J_G} & -\frac{C_r l_r^2 + C_f l_f^2}{J_G v_a} \end{bmatrix} x + \begin{bmatrix} \frac{C_f}{m_a v_a} \\ \frac{C_f l_f}{J_G} \end{bmatrix} u + \begin{bmatrix} \frac{C_r}{m_a v_a} \\ -\frac{C_r l_r}{J_G} \end{bmatrix} d_\delta \tag{15}$$

$$y = I_2 x$$

where $I_2$ is the 2-D identity matrix. The exact evolution of the disturbance $d_\delta$ during a lateral maneuver is difficult to capture as there is a complex interplay between the system kinematic structure, its dynamical parameters, and its response to lateral motion. Therefore, the disturbance $d_\delta$ will be affected by both the current system state $x$ as well as the static parameters of the system; with the shock absorber condition being among the latter category. To model the previously described effect of the disturbance $d_\delta$ on the lateral dynamics, it can be partitioned in two additive

25

contributions to yield the following state space model:

$$\dot{x} = \begin{bmatrix} \dot{\beta} \\ \ddot{\psi} \end{bmatrix} = \begin{bmatrix} -\frac{C_r + C_f}{m_a v_a} & -1 + \frac{C_r l_r - C_f l_f}{m_a v_a^2} \\ \frac{C_r l_r - C_f l_f}{J_G} & -\frac{C_r l_r^2 + C_f l_f^2}{J_G v_a} \end{bmatrix} x + \begin{bmatrix} \frac{C_f}{m_a v_a} \\ \frac{C_f l_f}{J_G} \end{bmatrix} u + \begin{bmatrix} \frac{C_r}{m_a v_a} \\ -\frac{C_r l_r}{J_G} \end{bmatrix} \left( \overline{d}_\delta + \hat{d}_\delta(x) \right) \tag{16}$$

$$y = I_2 x$$

where $\overline{d}_\delta$ collects the static effects due to system asymmetries, while $\hat{d}_\delta(x)$ collects the dynamical coupling of the disturbance with the system state. For simplicity, it can be assumed that $\hat{d}_\delta(x)$ has zero mean as the system should operate about the runway centerline and will be neglected in the subsequent analysis. In this way, the dominant term $\overline{d}_\delta$ and its relationship to shock absorber leakage-induced asymmetries in the lateral dynamics can be studied in isolation. The equilibrium of the previous system neglecting the disturbance $d_\delta$ will describe a circular movement. By working out the expression of the equilibrium steering input $\overline{\delta}_f$, the following relationship can be obtained:

$$\overline{\delta}_f = \frac{L}{R} \left( 1 + K_u v_a^2 \right) \tag{17}$$

where $R$ is the radius of the turn, and $K_u$ is the understeering gain, defined as the following expression:

$$K_u = \frac{m_a}{L^2} \left( \frac{l_r}{C_f} - \frac{l_f}{C_r} \right) \tag{18}$$

## B. Modified Bicycle Model

In the case of the Differential Braking Mode, the lateral stability analysis becomes more complex as the steering angle $\delta_f$ becomes an output of the system. However, a Modified Bicycle Model can be devised that is able to capture the most relevant lateral dynamics for this scenario. The assumptions and discussion about the model validity pointed out in Sec. III.A still apply to this case. The schematic representation of the Modified Bicycle Model main involved quantities is reported in Fig. 18.

With reference to Fig. 18, the aircraft is abstracted as a single-track vehicle of mass $m_a$ positioned at the center of gravity, which is located at a distance $l_r$ from the rear wheels axle and a distance $l_f$ from the front wheel center of rotation. The velocity vector of the full aircraft has a magnitude $v_a$ and describes a side-slip angle $\beta$ with respect to the longitudinal plane of the vehicle. The aircraft is turning at a yaw rate $\dot{\psi}$, while exhibiting a steering angle $\delta_f$ at the front wheel and subjected to a rear wheel disturbance steering angle $\delta_r$. The front wheel experiences a lateral force $F_f$, while the rear wheel experiences a lateral force $F_r$. The lateral acceleration of the aircraft will be denoted $a_y$ and its rotational
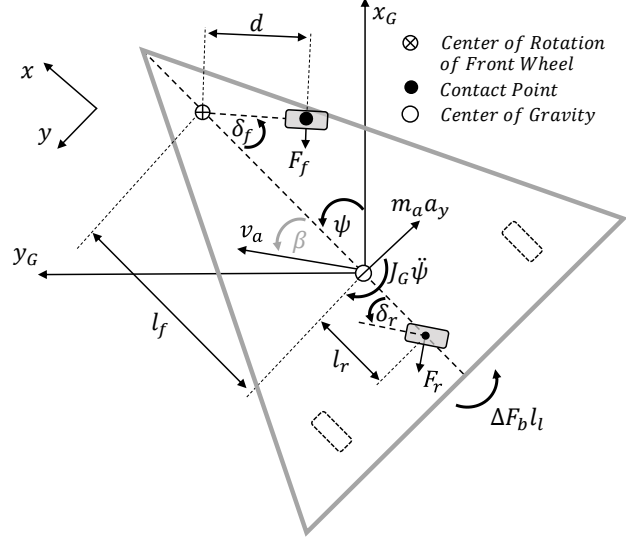
**Fig. 18 Schematic view of the Modified Bicycle Model with associated dynamic quantities and geometrical parameters.**

inertia will be designated $J_G$. A peculiarity of this operating mode arises from the fact that the contact point of the front wheel with the runway does not coincide with the front wheel rotational joint axis. Between them there is a distance $d$ that needs to be accounted for, as illustrated in Fig. 19. Moreover, an external moment $\Delta F_b l_l$ has been defined to account for the differential braking input generated between the right and left MLG wheels, with $l_l$ indicating half of the separation between both wheels in the MLG, $\Delta F_b = F_{xr} - F_{xl}$; and $F_{xr}$ and $F_{xl}$ denoting the generated longitudinal forces at the MLG right and left wheels by the braking action, respectively. The dynamic equations of the system are reported next, for which a small angle approximation has been used in their derivation:

$$m_a(\dot{\psi} + \dot{\beta})v_a = C_f\left(-\beta + \delta_f + \frac{-\dot{\psi}l_f + \dot{\delta}_f d}{v_a}\right) + C_r\left(-\beta + \frac{\dot{\psi}l_r}{v_a} + \delta_r\right)$$

(19a)

$$J_G\ddot{\psi} = C_f\left(l_f - d\right)\left(-\beta + \delta_f + \frac{-\dot{\psi}l_f + \dot{\delta}_f d}{v_a}\right) - C_r l_r\left(-\beta + \frac{\dot{\psi}l_r}{v_a} + \delta_r\right) + \Delta F_b l_l$$

(19b)

$$J_s\ddot{\delta}_f = -c_s\dot{\delta}_f - dC_f\left(-\beta + \delta_f + \frac{-\dot{\psi}l_f + \dot{\delta}_f d}{v_a}\right)$$

(19c)

The previous dynamic system can be obtained by performing three force/moment balances. Equation (19a) represents the lateral force balance along the local $y$ axis. Equation (19b) is obtained by performing a moment balance around the center of gravity of the aircraft. Equation (19c) represents the front wheel dynamics by the means of a moment balance
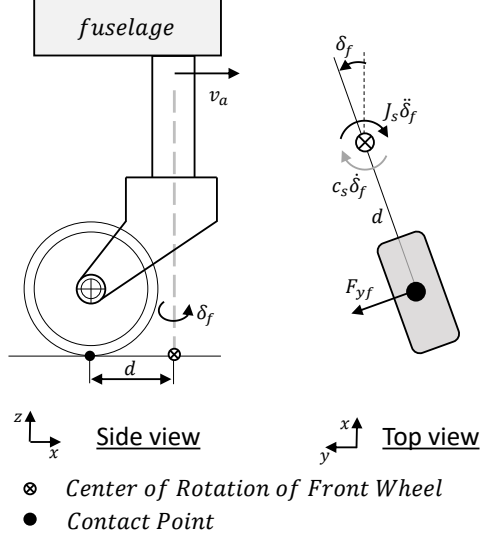
27

**Fig. 19 Schematic view of the NLG geometrical and dynamic quantities. Left: Side view highlighting the distance between the center of rotation and wheel contact point. Right: Top view highlighting the moments involved in the rotational joint.**

around the center of rotation of said wheel, where $J_s$ corresponds to the wheel rotational inertia of the front wheel, and $c_s$ represents the rotational damping of the joint at the front wheel. The terms $C_r$ and $C_f$ assume the same meaning as in the standard Bicycle Model.

Eqs. (19a), (19b), and (19c) can be arranged into standard state space format by proposing the differential braking force $\Delta F_b$ as an input $u$; the rear wheel steering angle $\delta_r$ as a disturbance $d_\delta$; and the side-slip angle $\beta$, the yaw rate $\dot{\psi}$, the front steering angle $\delta_f$, and the front steering angle rate $\dot{\delta}_f$ as states $x$ and outputs $y$. By simple algebraic manipulations, the following system may be obtained:

$$\dot{x} = \begin{bmatrix} -\frac{C_r+C_f}{m_a v_a} & -1+\frac{C_r^l-C_f^l}{m_a v_a^2} & \frac{C_f}{m_a v_a} & \frac{C_f^d}{m_a v_a^2} \\ \frac{C_r^l-C_f^l+C_f^d}{J_G} & -\frac{C_r^{2l}+C_f^{2l}-C_f^l d}{J_G v_a} & \frac{C_f^l-C_f^d}{J_G} & \frac{C_f^l d-C_f^{2d}}{J_G v_a} \\ 0 & 0 & 0 & 1 \\ \frac{C_f^d}{J_s} & \frac{C_f^l d}{J_s v_a} & -\frac{C_f^d}{J_s} & -\frac{C_f^{2d}+c_s v_a}{J_s v_a} \end{bmatrix} x + \begin{bmatrix} 0 \\ \frac{l_l}{J_G} \\ 0 \\ 0 \end{bmatrix} u + \begin{bmatrix} \frac{C_r}{m_a v_a} \\ -\frac{C_r^l}{J_G} \\ 0 \\ 0 \end{bmatrix} \left( \overline{d}_\delta + \hat{d}_\delta(x) \right) \qquad (20a)$$

$$y = I_4 x \qquad (20b)$$

where $I_4$ is the 4-D identity matrix, the same disturbance decomposition as done in Section III.A was conducted, and
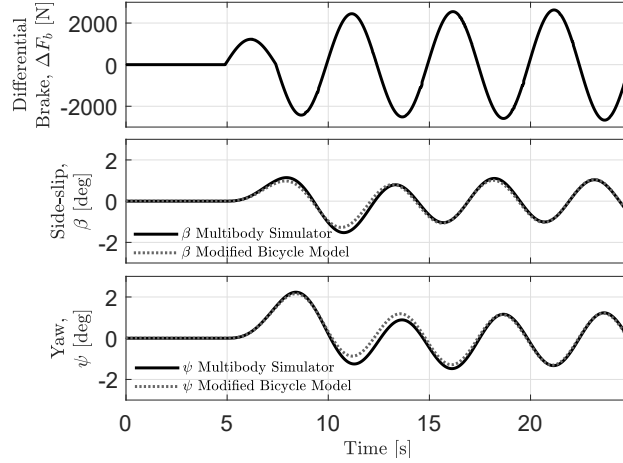
**Fig. 20 Comparison between the Multibody Simulator and Modified Bicycle Model in Differential Braking Mode for a maneuver performed at 100 km/h. Top: Differential braking input $\Delta F_b$. Middle: Aircraft body side-slip angle $\beta$. Bottom: Yaw $\psi$.**

the following definitions were adopted for notation compactness:

$$C_r^l = C_r l_r \quad C_r^{2l} = C_r l_r l_r \quad C_r^d = C_r d \tag{21a}$$

$$C_f^l = C_f l_f \quad C_f^{2l} = C_f l_f l_f \quad C_f^d = C_f d \tag{21b}$$

A comparison of the variables of interest between the results obtained from the previously defined Modified Bicycle Model against the Multibody Simulator can be appreciated in Fig. 20 and Fig. 21, where a sinusoidal differential braking input is applied at a velocity regime of 100 km/h. A clear match between the evolution of the illustrated system states is observed.
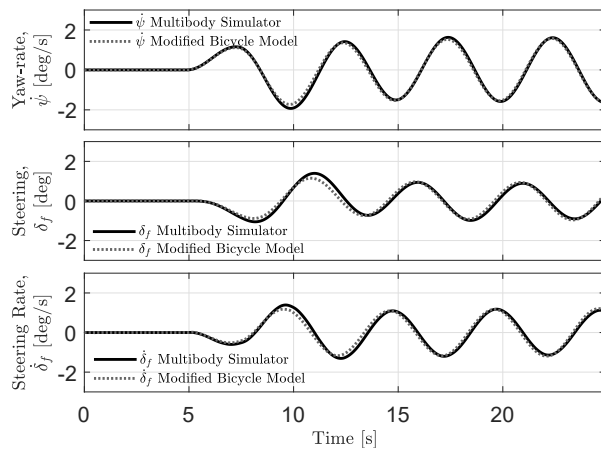
**Fig. 21 Comparison between the Multibody Simulator and Modified Bicycle Model in Differential Braking Mode for a maneuver performed at 100 km/h. Top: Yaw rate $\dot{\psi}$. Middle: Steering angle $\delta_f$. Bottom: Steering angle rate $\dot{\delta}_f$.**

**Table 3  Maneuvers performed for data generation in the Engaged Steering Mode**

| Preload Coefficient Scaling | Velocity [$km/h$] | Steering Excitation [°] | Thrust Force | Frequency Range [$Hz$] |
|---|---|---|---|---|
| 1.0 | 80/100/120 | 0.05 | ON | 0.1-1 |
| 0.9 | 80/100/120 | 0.05 | ON | 0.1-1 |
| 0.8 | 80/100/120 | 0.05 | ON | 0.1-1 |
| 0.7 | 80/100/120 | 0.05 | ON | 0.1-1 |
| 0.6 | 80/100/120 | 0.05 | ON | 0.1-1 |
| 0.5 | 80/100/120 | 0.05 | ON | 0.1-1 |

## IV. Sensitivity Analysis

In this section, the impact of the MLG shock absorber leakage on the lateral aircraft stability is discussed. For the data generation, a series of maneuvers that enable to excite the lateral dynamics were performed with the Multibody Simulator. The sensitivity to the MLG shock absorber leakage is explored by altering the preload coefficient in steps of -10%, reaching an extreme scenario of -50% preload scaling from a nominal condition, which can be considered a severe leakage. The experiments are repeated in three different speed regimes between 80 km/h up to 120 km/h. To perform the analysis, each of these maneuvers is then replicated with the analytical models by feeding the same input $u$ as the one from the Multibody Simulator. In each experiment, the constant disturbance $\overline{d}_\delta$ of the analytical models is adjusted to match the Multibody Simulator responses, as this input signal concentrates the uncertainty in the change in the dynamics due to the shock absorber leakage. The rest of the parameters required for the time simulation of the analytical models are left unperturbed according to the aircraft characteristics, or in the case of the aircraft body velocity $v_a$, selected appropriately for the scenario. This procedure allows the developed analytical models, that evolve in the planar yaw dimension, to incorporate dynamical changes in the vertical plane of the system. In the following subsections, both operating modes will be separately analyzed.

### A. Shock Absorber Leakage Impact on Engaged Steering Mode

For the Engaged Steering Mode analysis, the excitation for the maneuvers employed for data generation with the Multibody Simulator were sinusoidal sine sweeps at the front steering angle $\delta_f$. In this test, once the aircraft is accelerated to a required velocity $v_a$, a sinusoidal steering angle $\delta_f$ is applied with a linearly increasing frequency, while keeping the velocity $v_a$ as steady as possible by adjusting the thrust applied in the longitudinal axis. The selected amplitude of the steering angle was equal to 0.05°, with the maneuver performed in a Heavy aircraft inertial configuration in dry friction conditions. The frequency range covered by the steering excitation was selected to be between 0.1-1 Hz, as this is a common frequency range excited by a pilot operating the front steering actuator. The summary of the maneuvers performed for data generation are presented in Table 3. An example of such a maneuver with a nominal
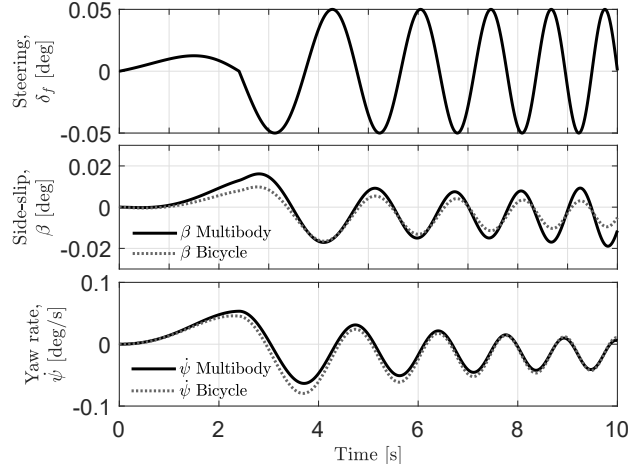
**Fig. 22 Comparison between the Multibody Simulator and Bicycle Model lateral dynamics for a sinusoidal sweep excitation at 100 km/h with a preload scaling coefficient of 1.0 for the right MLG shock absorber. Top: Steering angle $\delta_f$. Middle: Aircraft body side-slip angle $\beta$. Bottom: Yaw rate $\dot{\psi}$.**

shock absorber condition can be appreciated in Fig. 22, in which the comparison against the Bicycle Model is overlaid. As shown in Fig. 22, the maneuver follows the expected dynamics after the steering angle is applied. Note that the first lobe of the sinusoidal sweep excitation was selected to be one-fourth of the rest of the waveform to keep the aircraft evolution about the runway centerline. The biggest mismatch between both models is exhibited in the side-slip angle $\beta$, as the Bicycle Model underestimates this quantity. This can be explained due to the roll degree of freedom that induces an additional lateral motion as it couples with the steering excitation, which is neglected in the Bicycle Model as one of its simplifying assumptions. In any case, the Bicycle Model is able to replicate in a satisfactory manner the response of the Multibody Simulator for the purpose of the present analysis.

As an illustration of the effectiveness of the modelling approach proposed to capture the impact of the shock absorber leakage on the lateral aircraft dynamics, a maneuver including a -40% preload coefficient scaling at 120 km/h is also shown in Fig. 23. For convenience, the output of the Bicycle Model without the consideration of the proposed constant disturbance $\overline{d}_\delta$ is also overlaid. As can be appreciated in Fig. 23, the lateral deviation in the dynamics induced by the asymmetry in the MLG shock absorber condition is exposed and correctly captured by the input disturbance $\overline{d}_\delta$. The fitting procedure was repeated for the set of maneuvers detailed in Table 3 by identifying the level of disturbance $\overline{d}_\delta$ that yielded a match with the dynamics predicted by the Multibody Simulator. The identified disturbance levels are presented in Table 4. As expected, the disturbance $\overline{d}_\delta$ magnitude required to match the dynamics increases with an increasing shock absorber leakage. Moreover, there is a dependence of the leakage impact on the velocity of the system. As such, it is expected that the leakage influences the dynamics more severely at higher velocities. Further insight into the change in the lateral stability properties of the aircraft with a varying MLG shock absorber condition can be obtained by analyzing the frequency domain response of the Bicycle Model. In particular, a relevant transfer function
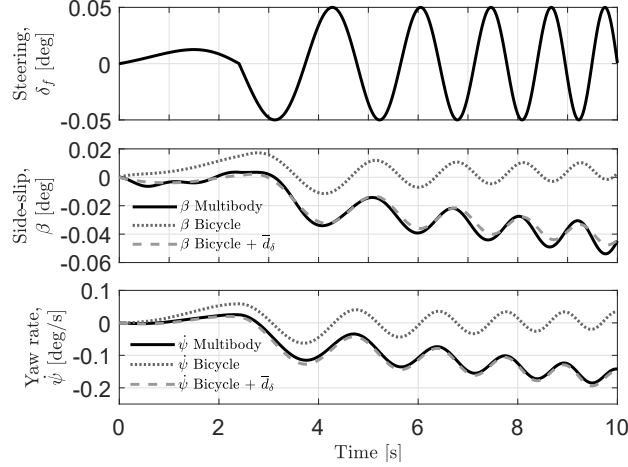
**Fig. 23** **Comparison between the Multibody Simulator and Bicycle Model lateral dynamics for a sinusoidal sweep excitation at 120 km/h with a preload scaling coefficient of 0.6 for the right MLG shock absorber. Top: Steering angle $\delta_f$. Middle: Aircraft body side-slip angle $\beta$. Bottom: Yaw rate $\dot{\psi}$.**

**Table 4** **Relationship between the constant disturbance $\overline{d}_\delta$ experienced by the aircraft due to an increasing right shock absorber MLG leakage across different velocities in Engaged Steering Mode**

| Preload Coefficient Scaling | $\overline{d}_\delta$ at 80 km/h | $\overline{d}_\delta$ at 100 km/h | $\overline{d}_\delta$ at 120 km/h |
|:---:|:---:|:---:|:---:|
| 1.0 | 0 | 0 | 0 |
| 0.9 | $0.10 \cdot 10^{-5}$ | $0.50 \cdot 10^{-5}$ | $1.00 \cdot 10^{-5}$ |
| 0.8 | $0.20 \cdot 10^{-5}$ | $1.00 \cdot 10^{-5}$ | $4.00 \cdot 10^{-5}$ |
| 0.7 | $0.30 \cdot 10^{-5}$ | $1.50 \cdot 10^{-5}$ | $6.00 \cdot 10^{-5}$ |
| 0.6 | $0.35 \cdot 10^{-5}$ | $1.50 \cdot 10^{-5}$ | $6.50 \cdot 10^{-5}$ |
| 0.5 | $0.40 \cdot 10^{-5}$ | $2.50 \cdot 10^{-5}$ | $7.00 \cdot 10^{-5}$ |

to look into is the one that maps the steering disturbance $d_\delta$ to the yaw rate $\dot{\psi}$, as it is directly related to the physical system response that the pilot can experience while trying to keep the aircraft to follow a prescribed yaw reference. The steering input disturbance $d_\delta$ to yaw rate $\dot{\psi}$ transfer function $G_{d_\delta}^{\dot{\psi}}(s)$ can be obtained from the state space representation of the system in Eq. (15). Performing the necessary transformations, the following expression is obtained:

$$G_{d_\delta}^{\dot{\psi}}(s) = -\left( \frac{C_r v_a}{J_G m_a v_a^2} \right) \left( \frac{l_r m_a v_a s + C_f L}{s^2 + a_1 s + a_2} \right) \tag{22a}$$

$$a_1 = \frac{1}{v_a} \left( \frac{C_r + C_f}{m_a} + \frac{C_r^{2l} + C_f^{2l}}{J_G} \right) \tag{22b}$$

$$a_2 = \left( \frac{C_r C_f L^2}{m_a J_G v_a^2} \right) (1 + K_u v_a^2) \tag{22c}$$

As indicated by Eq. (22a), the resulting transfer function is a second-order system with a single zero at the open left-half complex plane. In Fig. 24, the evolution of the transfer function with respect to speed can be observed.
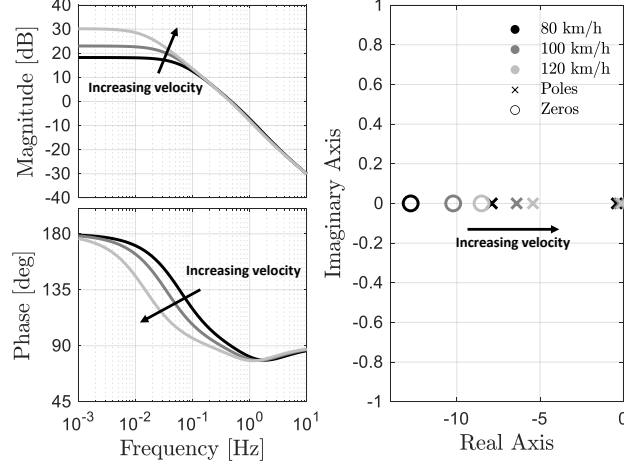
33

**Fig. 24 Evolution of the yaw rate transfer function $G_{d_\delta}^{\dot{\psi}}$ with varying speed. Left: Bode Plot. Right: Pole and Zero Plot.**

The plots shown in Fig. 24 indicate that a higher velocity will be associated to a degradation in the lateral stability of the aircraft while landing. Indeed, the Bode Plot shows that at higher velocities the disturbance $d_\delta$ gets magnified for low frequency and static effects, such as the ones induces by asymmetrical shock absorber leakages modelled by the signal $\overline{d}_\delta$. Moreover, from the Pole and Zero Plot, it is possible to see how at higher velocities the aircraft is closer to instability as the poles are pushed towards the right complex plane. This effect can be understood algebraically by the roots of the characteristic polynomial exposed in the denominator of $G_{d_\delta}^{\dot{\psi}}$. By performing some algebraic steps, the roots can be arranged in the following manner:

$$\lambda = -\frac{\alpha_\lambda}{2v_a} \pm \frac{1}{2m_a J_G v_a}\sqrt{\beta_\lambda + \gamma_\lambda v_a^2} \tag{23a}$$

$$\alpha_\lambda = \frac{C_r + C_f}{m_a} + \frac{C_r^{2l} + C_f^{2l}}{J_G} \tag{23b}$$

$$\beta_\lambda = \left((C_r + C_f)J_G + (C_r^{2l} + C_f^{2l})m_a\right)^2 - 4C_r C_f L^2 \tag{23c}$$

$$\gamma_\lambda = -4C_r C_f L^2 m_a J_G K_u \tag{23d}$$

where for the considered case study $\alpha_\lambda > 0$, $\beta_\lambda > 0$ and $\gamma_\lambda > 0$ are constants depending on the aircraft geometry and inertial characteristics. The first factor in Eq. (23a) determines the centroid of the pair of poles, which will be pushed rightwards with an increasing velocity $v_a$ while decreasing in absolute value. The second factor tends to stay relatively constant as there is a dependency in the order of $v_a$ for both the numerator and the denominator. When $v_a$ crosses some critical velocity $v_c$ threshold, instability will arise.

In this manner, as higher velocities are more critical for the lateral stability properties of the aircraft, a sensitivity analysis at the highest velocity considered, for varying shock absorber conditions, is worth pursuing. Hence, the
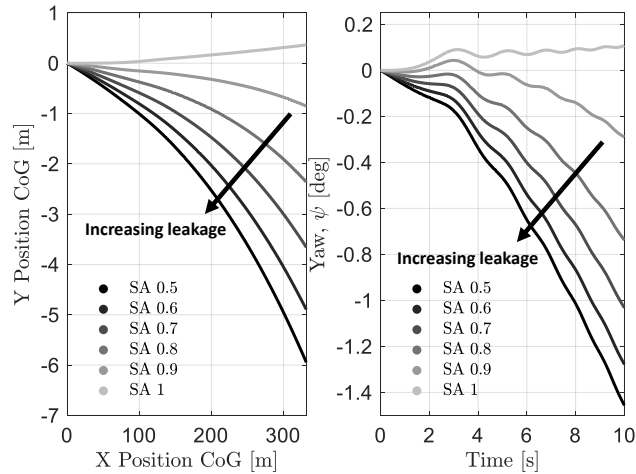
**Fig. 25 Evolution of dynamical quantities with varying shock absorber condition, for a sinusoidal sweep maneuver at 120 km/h. Left: Center of Gravity trajectory along the runway (note that the two axes are not in scale). Right: Yaw $\psi$.**

evolution of key dynamical quantities with varying shock absorber conditions at 120 km/h is presented in Fig. 25 and in Fig. 26. From Fig. 25, it can be appreciated that the aircraft trajectory gets noticeably affected by a varying shock absorber leakage. The asymmetry induced by a weaker right MLG shock absorber induces a moment that may interfere with the steering commands $\delta_f$ generated by the pilot while trying to keep the aircraft about the runway centerline. The same trend can be appreciated in Fig. 26 in terms of the state variables of the model.

Relating both trends observed, the previous observations mean that the most critical situation arises at the highest speeds with a shock absorber suffering from significant leakage. Not only the stability can become compromised, but the controllability of the system is degraded, making the yaw reference tracking task more complicated for the pilot.
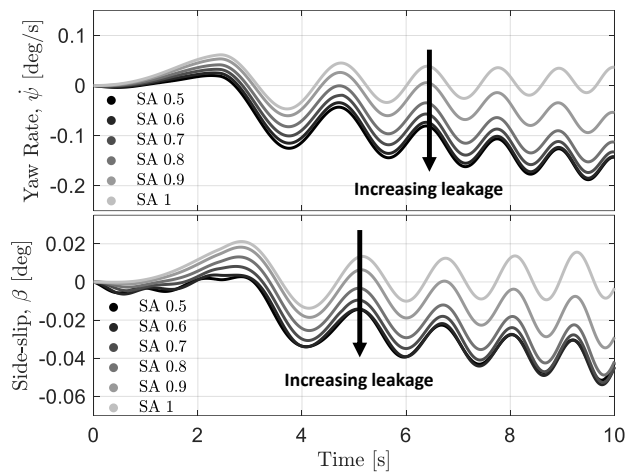
**Fig. 26    Evolution of dynamical quantities with varying shock absorber condition, for a sinusoidal sweep maneuver at 120 km/h. Top: Aircraft body side-slip angle $\beta$. Bottom: Yaw rate $\dot{\psi}$.**

**Table 5    Maneuvers performed for data generation in the Differential Braking Mode**

| Preload Coefficient Scaling | Velocity [$km/h$] | Differential Braking Excitation [$psi$] | Thrust Force | Frequency Range [$Hz$] |
|---|---|---|---|---|
| 1.0 | 80/100/120 | 200 | ON | 0.1-1 |
| 0.9 | 80/100/120 | 200 | ON | 0.1-1 |
| 0.8 | 80/100/120 | 200 | ON | 0.1-1 |
| 0.7 | 80/100/120 | 200 | ON | 0.1-1 |
| 0.6 | 80/100/120 | 200 | ON | 0.1-1 |
| 0.5 | 80/100/120 | 200 | ON | 0.1-1 |

## B. Shock Absorber Leakage Impact on Differential Braking Mode

The Modified Bicycle Model from Sec. III.B allows to perform a similar analysis in the case of the Differential Braking mode operation, as the one performed in Sec. IV.A. However, in the case of the Modified Bicycle Model, there is no analogous quantity to the understeering gain $K_u$. Moreover, the characteristic polynomial of the system represented by Eqs. (20a) and (20b) is of fourth-order, and hence, its explicit solution is highly complex and provides little insight into the system sensitivity to parameters. Because of these reasons, only a graphical frequency domain analysis will be performed by relying on the rear steering disturbance $d_\delta$ to yaw rate $\dot{\psi}$ transfer function, also denoted $G_{d_\delta}^{\dot{\psi}}(s)$, which can be obtained by standard system transformations applied to Eqs. (20a) and (20b).

Again, the parameters under study will be the velocity $v_a$ and the shock absorber condition, which can be accounted for with a suitable identification of the constant disturbance $\overline{d}_\delta$ that produces a match between the Multibody Simulator output and the analytical Modified Bicycle Model. An important aspect to highlight in the Differential Braking operation mode, is that the NLG wheel steering damping conditions are particularly relevant to the evolution of the dynamics with a varying shock absorber leakage. For this reason, the study will be performed in two regimes: Lightly Damped front wheel steering, and Heavily Damped front wheel steering, the latter of which is the most commonly found in the case study. The difference between the two cases will only lie in the parameter selected for the front rotational joint damping value $c_s$.

In this operating mode, the maneuvers selected for the analysis are also sinusoidal sweeps of linearly increasing frequency between 0.1-1 Hz in three different speed regimes between 80-120 km/h. The selected amplitude applied at the braking actuators was 200 psi. The summary of the analyzed conditions for the Differential Braking Mode can be found in Table 5.

### 1. Lightly Damped NLG Case

A representative maneuver comparing the Multibody Simulator dynamics against the proposed analytical Modified Bicycle Model with a -40% preload coefficient scaling at 80 km/h is shown in Fig. 27. and Fig. 28. For convenience,
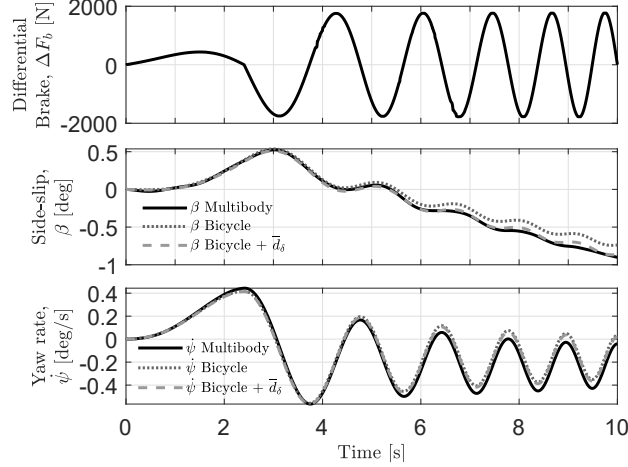
**Fig. 27 Comparison between the Multibody Simulator and Modified Bicycle Model lateral dynamics for a sinusoidal sweep differential braking excitation at 80 km/h with a preload scaling coefficient of 0.6 for the right MLG shock absorber. Top: Differential braking input $\Delta F_b$. Middle: Aircraft body side-slip angle $\beta$. Bottom: Yaw rate $\dot{\psi}$.**

**Table 6 Relationship between the constant disturbance $\overline{d}_\delta$ experienced by the aircraft due to an increasing right shock absorber MLG leakage across different velocities in Differential Braking Mode, lightly damped case**

| Preload Coefficient Scaling | $\overline{d}_\delta$ at 80 km/h | $\overline{d}_\delta$ at 100 km/h | $\overline{d}_\delta$ at 120 km/h |
|---|---|---|---|
| 1.0 | 0 | 0 | 0 |
| 0.9 | $0.30 \cdot 10^{-3}$ | $0.30 \cdot 10^{-3}$ | $0.30 \cdot 10^{-3}$ |
| 0.8 | $0.70 \cdot 10^{-3}$ | $0.90 \cdot 10^{-3}$ | $0.70 \cdot 10^{-3}$ |
| 0.7 | $1.0 \cdot 10^{-3}$ | $1.00 \cdot 10^{-3}$ | $1.00 \cdot 10^{-3}$ |
| 0.6 | $1.3 \cdot 10^{-3}$ | $1.20 \cdot 10^{-3}$ | $1.50 \cdot 10^{-3}$ |
| 0.5 | $1.5 \cdot 10^{-3}$ | $1.50 \cdot 10^{-3}$ | $1.50 \cdot 10^{-3}$ |

the output of the Modified Bicycle Model without the consideration of the proposed constant disturbance $\overline{d}_\delta$ is also overlaid. The lateral deviation in the dynamics induced by the asymmetry in the MLG shock absorber condition is again correctly captured by the proposed input disturbance $\overline{d}_\delta$.

The fitting procedure was repeated for the set of maneuvers detailed in Table 5 by identifying the level of disturbance $\overline{d}_\delta$ that yielded a match with the dynamics predicted by the Multibody Simulator. The identified disturbance levels are presented in Table 6. As expected, the disturbance $\overline{d}_\delta$ magnitude required to match the dynamics increases with an increasing shock absorber leakage. In this scenario, no evident correlation with the aircraft velocity is appreciated.

The evolution of $G_{d_\delta}^{\dot{\psi}}(s)$ with respect to velocity, for a lightly damped NLG steering wheel, is exposed in Fig. 29. As can be appreciated from Fig. 29, the same stability degradation trend as the one observed in the Engaged Steering mode can be evidenced in this situation. Even though the dynamics are more complex, a higher velocity drags all the poles and zeros towards the right complex plane. Moreover, an interesting behavior can be appreciated in the Bode Plot
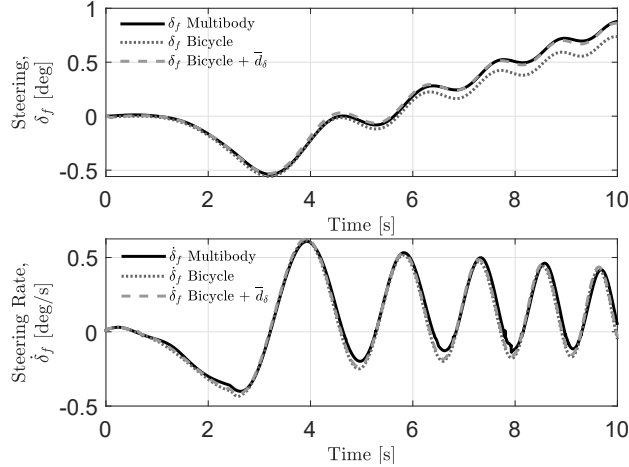
**Fig. 28  Comparison between the Multibody Simulator and Modified Bicycle Model lateral dynamics for a sinusoidal sweep differential braking excitation at 80 km/h with a preload scaling coefficient of 0.6 for the right MLG shock absorber. Top: Steering angle $\delta_f$. Bottom: Steering angle rate $\dot{\delta}_f$.**

that was not present in the Engaged Steering mode. At high velocities, the presence of a peak at around 0.02 [Hz] is quite evident, due to a pair of underdamped complex conjugate poles. These underdamped poles can be associated to the nose wheel steering dynamics. Since there is a non-zero front rotational joint damping $c_s$, during a differential braking lateral excitation a misalignment is generated between the body and front wheel velocity vectors. Before the system can achieve a steady state, the oscillations generated at the front wheel would need to settle down. As the peak exists in the vicinity of frequencies normally excited by a yaw lateral controller, it highlights an important difficulty that should be managed at high velocity regimes.

As higher velocities are more critical for the lateral stability properties of the aircraft, a sensitivity analysis at the highest velocity considered, for varying shock absorber conditions, is presented in Fig. 30 and Fig. 31. From Fig. 30, and similarly to the Engaged Steering Mode leakage sensitivity analysis, it can be appreciated that the aircraft trajectory gets affected by the shock absorber leakage at the right MLG. In this manner, due to the asymmetric leakage, the aircraft would naturally tend to turn to the right; in other words, the pilot would need to apply a higher command to the left to overcome the observed asymmetric effect. However, in the operating condition tested the yaw rate $\dot{\psi}$ seems less sensitive to leakage variations compared to the Engaged Steering Mode. Instead, from Fig. 31, the aircraft body side-slip angle $\beta$ is considerably affected by the increasing leakage condition. The asymmetry is also propagated to the steering angle $\delta_f$, which is free to evolve in the Engaged Steering Mode.
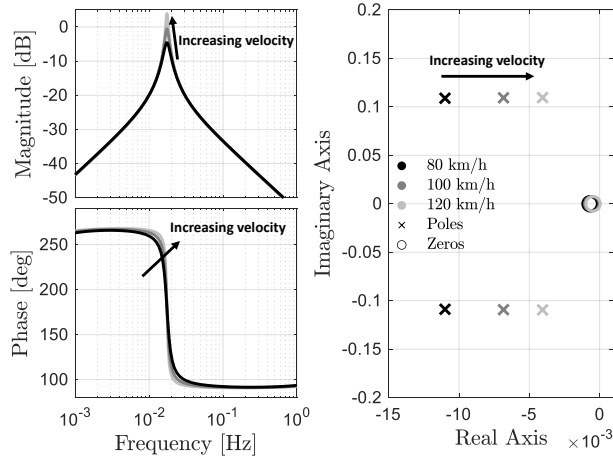
**Fig. 29** **Evolution of the yaw rate transfer function** $G_{d_\delta}^{\dot\psi}(s)$ **with varying speed and a lightly damped NLG. Left: Bode Plot. Right: Pole and Zero Plot. Only the dominant poles and zeros are highlighted.**
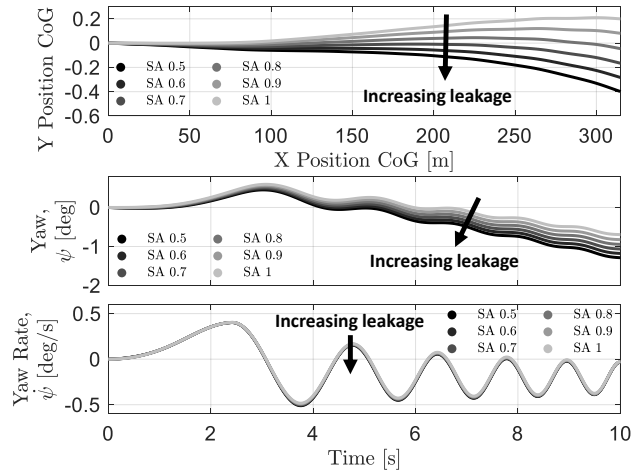


**Fig. 30** **Evolution of dynamical quantities with varying shock absorber condition, for a sinusoidal sweep differential braking maneuver at 120 km/h. Top: Center of Gravity trajectory along the runway (note that the two axes are not in scale). Middle: Yaw $\psi$. Bottom: Yaw rate $\dot\psi$.**
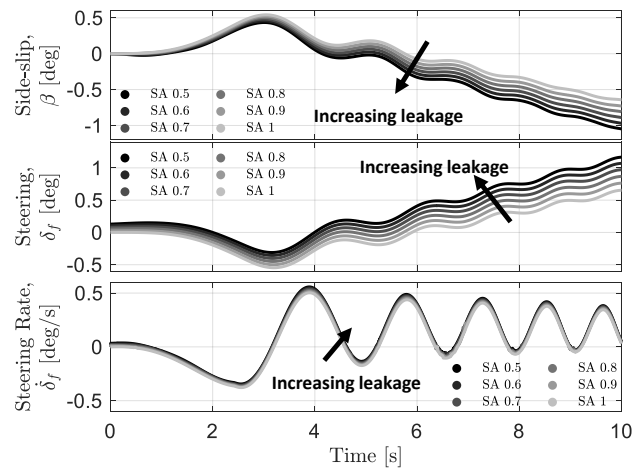
**Fig. 31  Evolution of dynamical quantities with varying shock absorber condition, for a sinusoidal sweep differential braking maneuver at 120 km/h. Top: Aircraft body side-slip angle $\beta$. Middle: Steering angle $\delta_f$. Bottom: Steering angle rate $\dot{\delta}_f$.**

**Table 7** **Relationship between the constant disturbance $\overline{d}_\delta$ experienced by the aircraft due to an increasing right shock absorber MLG leakage across different velocities in Differential Braking Mode, heavily damped case**

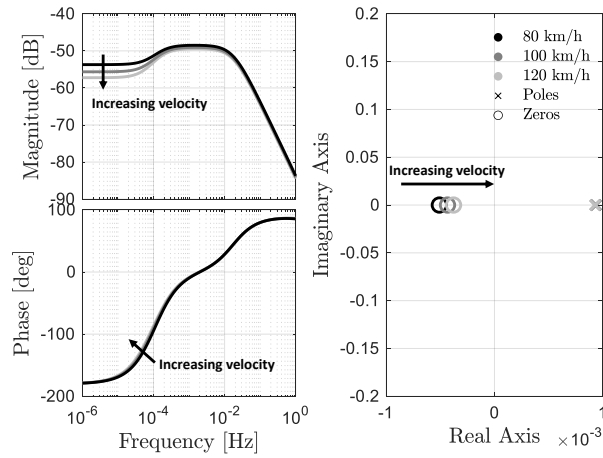| Preload Coefficient Scaling | $\overline{d}_\delta$ at 80 km/h | $\overline{d}_\delta$ at 100 km/h | $\overline{d}_\delta$ at 120 km/h |
|:---:|:---:|:---:|:---:|
| 1.0 | 0 | 0 | 0 |
| 0.9 | $0.10 \cdot 10^{-1}$ | $0.30 \cdot 10^{-1}$ | $0.20 \cdot 10^{-1}$ |
| 0.8 | $0.20 \cdot 10^{-1}$ | $0.50 \cdot 10^{-1}$ | $0.50 \cdot 10^{-1}$ |
| 0.7 | $0.25 \cdot 10^{-1}$ | $0.70 \cdot 10^{-1}$ | $1.00 \cdot 10^{-1}$ |
| 0.6 | $0.40 \cdot 10^{-1}$ | $1.10 \cdot 10^{-1}$ | $1.30 \cdot 10^{-1}$ |
| 0.5 | $0.50 \cdot 10^{-1}$ | $1.30 \cdot 10^{-1}$ | $1.50 \cdot 10^{-1}$ |



**Fig. 32** **Evolution of the yaw rate transfer function $G_{d_\delta}^{\dot{\psi}}(s)$ with varying speed and a heavily damped NLG. Left: Bode Plot. Right: Pole and Zero Plot. Only the dominant poles and zeros are highlighted.**

*2. Heavily Damped NLG Case*

Similarly as in Section IV.B.1, the fitting procedure for the set of maneuvers detailed in Table 5 in the case of a heavily damped NLG was conducted by identifying the level of disturbance $\overline{d}_\delta$ that yielded a match with the dynamics predicted by the Multibody Simulator. The identified disturbance levels are presented in Table 7. Same as in the previous scenarios considered, the disturbance $\overline{d}_\delta$ magnitude required to match the dynamics increases with an increasing shock absorber leakage. However, there is a stronger correlation with the aircraft velocity compared with the lightly damped Differential Braking case.

Next, the evolution of $G_{d_\delta}^{\dot{\psi}}(s)$ with respect to velocity, for a heavily damped NLG steering wheel, is exposed in Fig. 32. As can be appreciated from Fig. 32, the most noteworthy characteristic observed is that the dominant poles have moved to the instability region due to the increased NLG damping. The previous effect is highly undesirable as the task of maintaining the aircraft about the centerline during a braking maneuver can get significantly more difficult for the pilot and degrade lateral stability. An intuitive explanation for the impact of the heavily damped NLG effect can be
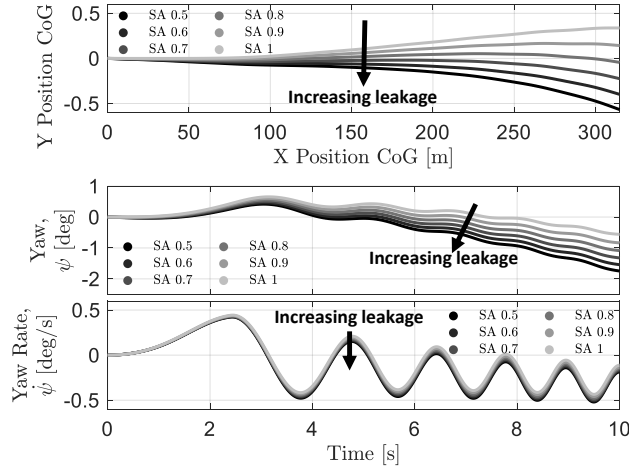
**Fig. 33 Evolution of dynamical quantities with varying shock absorber condition, for a sinusoidal sweep differential braking maneuver at 120 km/h. Top: Center of Gravity trajectory along the runway (note that the two axes are not in scale). Middle: Yaw $\psi$. Bottom: Yaw rate $\dot{\psi}$.**

attributed to the reduced compliance of the NLG steering angle $\delta_f$ to the aircraft yaw angle $\psi$ variations caused by the differential braking input. Hence, higher side-slip angles $\alpha_f$ are generated at the front wheel, causing the existence of higher lateral front wheel forces $F_f$.

Finally, a sensitivity analysis at the highest velocity considered, for varying shock absorber conditions, is presented in Fig. 33 and Fig. 34. From Fig. 33, it can be appreciated that the aircraft trajectory gets similarly affected by the shock absorber leakage at the right MLG as in the lightly damped condition, albeit with an increased effect in terms of magnitude. From Fig. 34, it is observed that again the aircraft body side-slip angle $\beta$ is considerably affected by the increasing leakage condition, whereas the steering angle $\delta_f$ also shows a bigger spread across the different conditions tested.

From the previous observations, and comparing against the sensitivity analysis conducted in Section IV.B.1, it can be concluded that the shock absorber leakage has a more pronounced effect on the lateral aircraft dynamics in the heavily damped NLG scenario. Both the equivalent disturbance $\overline{d}_\delta$ and the spread of the evolution of the lateral dynamical quantities across different shock absorber conditions are more prominent. Therefore, the most critical situation for lateral stability can be linked to a heavily damped NLG with a maximum shock absorber leakage during high velocity maneuvers.
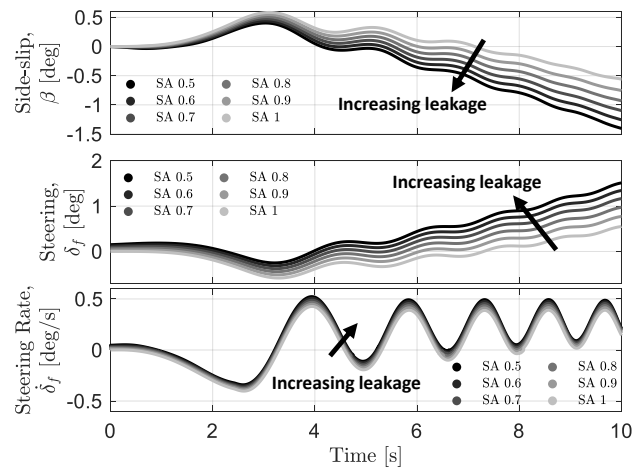
**Fig. 34** **Evolution of dynamical quantities with varying shock absorber condition, for a sinusoidal sweep differential braking maneuver at 120 km/h. Top: Aircraft body side-slip angle $\beta$. Middle: Steering angle $\delta_f$. Bottom: Steering angle rate $\dot{\delta}_f$.**

## V. Concluding Remarks

In this paper, the relationship between aircraft lateral stability and Main Landing Gear shock absorber leakage during on-ground braking maneuvers was studied. The analysis was conducted in a MATLAB Simulink simulation environment, by constructing a detailed multibody representation of a typical trainer aircraft endowed with a tricycle landing gear to study the system in different leakage conditions across a variety of velocity regimes. Two analytical models, able to replicate each operating mode considered, were proposed as a way of quantifying the shock absorber leakage impact by the means of a model augmentation with a constant disturbance lumped at the rear wheel.

The analysis allows to establish a link between Main Landing Gear shock absorber gas leakage and lateral stability degradation. In particular, for the case of the Engaged Steering mode, by analyzing the associated Bicycle Model, it was found that an asymmetrical gas leakage can be reproduced by introducing a rear wheel steering disturbance acting during the maneuver, which makes the control task more challenging for the pilot. The frequency domain analysis revealed a destabilizing effect at increasing velocities. For the case of the Differential Braking operation mode, by analyzing the associated Modified Bicycle Model, it was found that a similar destabilizing effect was present at higher speeds, with the shock absorber leakage relationship with controllability particularly relevant when considering heavily damped nose wheel steering conditions. The lateral stability degradation in heavily damped nose wheel steering conditions can be explained due to the reduced compliance of the front wheel steering angle rotation to differential braking inputs, inducing higher lateral wheel slip angles.

The findings of the conducted investigation make clear that an early diagnosis of the shock absorber condition would be significantly helpful in avoiding the negative consequences associated to the degradation of this component, as appropriate action could be taken before the lateral stability becomes compromised too significantly, which in turn would have an impact on the operational safety of the aircraft.

## References

[1] Ossa, E. A., and Paniagua, M., "Chapter 8 - Suspension and landing gear failures," *Handbook of Materials Failure Analysis with Case Studies from the Aerospace and Automotive Industries*, edited by A. S. H. Makhlouf and M. Aliofkhazraei, Butterworth-Heinemann, Boston, 2016, pp. 167–190. https://doi.org/10.1016/B978-0-12-800950-5.00008-9.

[2] Yang, H., Wan, F., and Cui, W., "Failure simulation and identification of shock absorber in carrier-based aircraft landing gear," *2016 International Conference on Prognostics and Health Management (ICPHM)*, 2016, pp. 1–6. https://doi.org/10.1109/ICPHM.2016.7542833.

[3] Haider, S., "Overview of Prognostics and Health Management for Landing Gear Maintenance," *2019 Annual Symposium on Reliability and Maintainability (RAMS)*, 2019, pp. 1–7. https://doi.org/10.1109/RAMS.2019.8768977.

[4] Correia, D., and Ferreira, A., "Aircrafts On-Ground Dynamics Models and Simulation Software: State-of-the-Art," *Sustainability*, Vol. 13, No. 16, 2021. https://doi.org/10.3390/su13169147.

[5] Klyde, D. H., Myers, T. T., Magdaleno, R. E., and Reinsberg, J. G., "Identification of the Dominant Ground Handling Characteristics of a Navy Jet Trainer," *Journal of Guidance, Control, and Dynamics*, Vol. 25, No. 3, 2002, pp. 546–552. https://doi.org/10.2514/2.4915.

[6] Klyde, D. H., Myers, T., Lampton, A. K., Draper-Donley, M., and Bishop, M., "Improved Models for the Ground Handling Assessment of Navy Aircraft," *AIAA Atmospheric Flight Mechanics Conference*, 2015, pp. 1–14. https://doi.org/10.2514/6.2015-0241.

[7] Georgieva, K., and Serbezov, V., "Mathematical model of aircraft ground dynamics," *2017 International Conference on Military Technologies (ICMT)*, 2017, pp. 514–519. https://doi.org/10.1109/MILTECHS.2017.7988812.

[8] Rankin, J., Coetzee, E., Krauskopf, B., and Lowenberg, M., "Bifurcation and Stability Analysis of Aircraft Turning on the Ground," *Journal of Guidance, Control, and Dynamics*, Vol. 32, No. 2, 2009, pp. 500–511. https://doi.org/10.2514/1.37763.

[9] Rankin, J., Krauskopf, B., Lowenberg, M., and Coetzee, E., "Operational Parameter Study of Aircraft Dynamics on the Ground," *Journal of Computational and Nonlinear Dynamics*, Vol. 5, No. 2, 2010. https://doi.org/10.1115/1.4000797.

[10] Dixon, J. C., *The shock absorber handbook, 2nd edition*, John Wiley & Sons, 2007. https://doi.org/10.1002/9780470516430, ISBN 978-0-470-51020-9.

[11] Weispfenning, T., "Fault Detection and Diagnosis of Components of the Vehicle Vertical Dynamics," *Meccanica*, Vol. 32, 1997, pp. 459–472. https://doi.org/10.1023/A:1004212001768.

[12] Hamed, M., Tesfa, B., Gu, F., and Ball, A., "A study of the suspension system for the diagnosis of dynamic characteristics," *2014 20th International Conference on Automation and Computing*, 2014, pp. 152–157. https://doi.org/10.1109/IConAC.2014.6935478.

[13] Yadav, D., and Ramamoorthy, R. P., "Nonlinear Landing Gear Behavior at Touchdown," *Journal of Dynamic Systems, Measurement, and Control*, Vol. 113, No. 4, 1991, pp. 677–683. https://doi.org/10.1115/1.2896474.

[14] Fazeli, A. M., Cepic, A., and Reber, S. M., *Servicing monitoring system for mixed fluid-gas shock struts*, 2016. US Patent 9285007.

[15] Rahmani, M., and Kamran, B., "Investigation on the Effect of Coulomb Friction on Nose Landing Gear Shimmy," *Journal of Vibration and Control*, Vol. 25, No. 2, 2019, pp. 255–272. https://doi.org/10.1177/1077546318774440.

[16] Miller, S., *Simscape Multibody Contact Forces Library*, 2021. URL https://github.com/mathworks/Simscape-Multibody-Contact-Forces-Library/releases/tag/21.1.5.0, Last Accessed: 2021-11-02.

[17] Fiala, E., "Seitenkraften am rollenden Luftreifen (Lateral Forces on Rolling Pneumatic Tires)," *Zeitschrift des Vereines Deutscher Ingenieure (V.D.I.) (Journal of the Association of German Engineers)*, Vol. 96, No. 29, 1954, pp. 973–979.

[18] Pacejka, H. B., *Tire and Vehicle Dynamics, 3rd edition*, Butterworth-Heinemann, 2012. https://doi.org/10.1016/C2010-0-68548-8, ISBN 978-0-08-097016-5.

[19] Burckhardt, M., *Fahrwerktechnik: Radschlupf-Regelsysteme (Chassis technology: Wheel slip control systems)*, Vogel Verlag, Wüzburg, Germany, 1993. ISBN 978-3-80-230477-4.

[20] D'Avico, L., Tanelli, M., and Savaresi, S., "Experimental validation of landing-gear dynamics for anti-skid control design," *2018 European Control Conference (ECC)*, 2018, pp. 2751–2756. https://doi.org/10.23919/ECC.2018.8550258.

[21] Peng, T., Yan, Q., Li, G., Zhang, X., Wen, Z., and Jin, X., "The braking behaviors of Cu-based metallic brake pad for high-speed train under different initial braking speed," *Tribology Letters*, Vol. 65, No. 4, 2017, pp. 1–13. https://doi.org/10.1007/s11249-017-0914-9.

[22] Fan, S., Zhang, L., Cheng, L., Tian, G., and Yang, S., "Effect of braking pressure and braking speed on the tribological properties of C/SiC aircraft brake materials," *Composites Science and Technology*, Vol. 70, No. 6, 2010, pp. 959–965. https://doi.org/10.1016/j.compscitech.2010.02.012.

[23] Ostermeyer, G., "On the dynamics of the friction coefficient," *Wear*, Vol. 254, No. 9, 2003, pp. 852–858. https://doi.org/10.1016/S0043-1648(03)00235-7.

[24] Ricciardi, V., Travagliati, A., Schreiber, V., Klomp, M., Ivanov, V., Augsburg, K., and Faria, C., "A novel semi-empirical dynamic brake model for automotive applications," *Tribology International*, Vol. 146, 2020, p. 106223. https://doi.org/10.1016/j.triboint.2020.106223.

[25] Yu, S., Chen, J., Huang, Q., Xiong, X., Chang, T., and Li, Y., "Effect of Braking Speeds on the Tribological Properties of Carbon/Carbon Composites," *Materials Transactions*, Vol. 51, No. 5, 2010, pp. 1038–1043. https://doi.org/10.2320/matertrans.M2009390.

[26] Gualdi, S., Morandini, M., and Ghiringhelli, G. L., "Anti-skid induced aircraft landing gear instability," *Aerospace Science and Technology*, Vol. 12, No. 8, 2008, pp. 627–637. https://doi.org/https://doi.org/10.1016/j.ast.2008.02.002.

[27] Milwitzky, B., and Cook, F. E., "Analysis of Landing-Gear Behavior," *NACA-TR-1154*, 1953, pp. 1–45.

[28] Evans, P., Perhinschi, M., and Mullins, S., "Modeling and Simulation of a Tricycle Landing Gear at Normal and Abnormal Conditions," *AIAA Modeling and Simulation Technologies Conference*, 2010, pp. 1–20. https://doi.org/10.2514/6.2010-7618.

[29] Pauwelussen, J., *Essentials of vehicle dynamics*, Butterworth-Heinemann, 2015. https://doi.org/https://doi.org/10.1016/C2014-0-00503-5, ISBN 978-0-08-100036-6.

[30] Savaresi, S., and Tanelli, M., *Active Braking Control Systems Design for Vehicles*, Springer-Verlag, London, UK, 2010. https://doi.org/10.1007/978-1-84996-350-3, ISBN 978-1-84996-350-3.